# Physics of Changes in Synoptic Midlatitude Temperature Variability

TAPIO SCHNEIDER AND TOBIAS BISCHOFF

*ETH Zurich, Zurich, Switzerland, and California Institute of Technology, Pasadena, California*

HANNA PŁOTKA

*ETH Zurich, Zurich, Switzerland*

## ABSTRACT

This paper examines the physical processes controlling how synoptic midlatitude temperature variability near the surface changes with climate. Because synoptic temperature variability is primarily generated by advection, it can be related to mean potential temperature gradients and mixing lengths near the surface. Scaling arguments show that the reduction of meridional potential temperature gradients that accompanies polar amplification of global warming leads to a reduction of the synoptic temperature variance near the surface. This is confirmed in simulations of a wide range of climates with an idealized GCM. In comprehensive climate simulations (CMIP5), Arctic amplification of global warming similarly entails a large-scale reduction of the near-surface temperature variance in Northern Hemisphere midlatitudes, especially in winter. The probability density functions of synoptic near-surface temperature variations in midlatitudes are statistically indistinguishable from Gaussian, both in reanalysis data and in a range of climates simulated with idealized and comprehensive GCMs. This indicates that changes in mean values and variances suffice to account for changes even in extreme synoptic temperature variations. Taken together, the results indicate that Arctic amplification of global warming leads to even less frequent cold outbreaks in Northern Hemisphere winter than a shift toward a warmer mean climate implies by itself.

## 1. Introduction

It has recently been argued that the amplified Arctic warming that accompanies global warming should increase the amplitude of large-scale eddies in the midlatitude atmosphere (Francis and Vavrus 2012; Liu et al. 2012). Arctic amplification of global warming is robustly seen in climate simulations and in observations of the past decades (Manabe and Wetherald 1980; Schneider and Held 2001; Holland and Bitz 2003; Graversen et al. 2008; Screen and Simmonds 2010; Serreze and Barry 2011; Masson-Delmotte et al. 2013; Collins et al. 2013; Cohen et al. 2014). The attendant reduction of the equator-to-pole surface temperature contrast in the Northern Hemisphere, the argument goes, implies a weakened upper-level jet stream by thermal wind balance. The weakened jet stream, in turn, is to become more "wavy," and midlatitude eddies are to propagate

more slowly and have larger amplitudes, as measured, for example, by meridional displacements of geopotential height contours. The slower and higher-amplitude eddies would then entail an increased probability of blocking episodes and extreme weather in midlatitudes of the Northern Hemisphere, including, for example, an increased frequency of cold outbreaks—although the globe overall is warming (Francis and Vavrus 2012; Liu et al. 2012). This argument has received widespread prominence (Kintisch 2014; Cohen et al. 2014). Over the course of winter 2013/14, during which central and eastern North America saw strong cold outbreaks that each lasted several days, it was ubiquitous in the media, including, for example, in a video released by the White House (Holdren 2014).

However, although the recent global warming is clearly amplified in the Arctic, especially during the cold season (Schneider and Held 2001; Graversen et al. 2008; Screen and Simmonds 2010; Serreze and Barry 2011; Cohen et al. 2014), observations do not show that this has changed amplitudes or phase speeds of midlatitude eddies (Screen and Simmonds 2013b; Barnes 2013;

*Corresponding author address:* Tapio Schneider, ETH Zurich, Sonneggstr. 5, 8092 Zurich, Switzerland.
E-mail: tapio@ethz.ch

Wallace et al. 2014; Screen 2014). The frequency of blocking in the Northern Hemisphere also has not changed appreciably (Barnes et al. 2014). Observed changes in temperature extremes that are coherent across midlatitudes can largely be explained by the shift toward higher mean temperatures, which entails changes in the frequency with which fixed temperature thresholds are crossed: cold outbreaks, understood as episodes when temperatures fall below a fixed cold threshold, occur less frequently as the climate warms; heat waves, understood as episodes when temperatures rise above a fixed warm threshold, occur more frequently (Easterling et al. 2000; Donat and Alexander 2012; Hansen et al. 2012; de Vries et al. 2012; Rhines and Huybers 2013; Peterson et al. 2013; Tingley and Huybers 2013; Coumou et al. 2013; Huntingford et al. 2013). Over some continental regions, temperature–soil moisture interactions, among other processes, may amplify summer heat waves (Schär et al. 2004; Seneviratne et al. 2006, 2010; Fischer and Schär 2009). But to the extent large-scale changes in temperature variability have been observed, in the cold seasons they point to a reduced variance on synoptic time scales in midlatitudes (Screen 2014), in agreement with simulations of warming climates (Kitoh and Mukano 2009; Ylhäisi and Räisänen 2014; Screen et al. 2015). The reduced temperature variance suggests cold outbreaks occur even less frequently than a shift toward warmer mean temperatures implies by itself.

Here, we present physical arguments that show that a reduced midlatitude temperature variance on synoptic time scales is generally to be expected from polar amplification of global warming. We provide a dynamical null hypothesis and scaling theory for how the midlatitude temperature variance changes as the climate warms, test the scaling theory with simulations with an idealized general circulation model (GCM), and demonstrate its broad consistency with comprehensive climate simulations. Using observations and simulations, we show that the probability density function (PDF) of synoptic temperature variations in midlatitudes is essentially Gaussian, so that changes in the mean and variance suffice to account for changes in extremes—at least to the extent these changes are currently identifiable. With the idealized GCM simulations, we also examine the hypothesis that polar amplification of global warming may lead to an increasing frequency of midlatitude temperature extremes through resonant amplification of synoptic transient eddies that more frequently become trapped in stationary waveguides (Petoukhov et al. 2013). Throughout the paper, we will focus on temperature variations on the synoptic time scales that are of primary importance for heat waves and cold outbreaks. We bandpass filter temperature variations to

time scales of 3–15 days, a band that includes relatively low-frequency synoptic variations to capture persistent temperature extremes. However, all results are essentially unchanged when bandpass filtering to more traditional synoptic time scales (e.g., 2–10 days).

## 2. Theory

### a. Potential temperature variance

For theoretical considerations, it is more convenient to consider potential temperature rather than temperature, because potential temperature is materially conserved in adiabatic airmass displacements. Airmass displacements may be assumed to be approximately adiabatic on synoptic time scales (which are shorter than radiative time scales) near the top of the planetary boundary layer, where boundary layer turbulent fluxes are weak. That is, synoptic potential temperature variations $\theta' = \theta - \overline{\theta}$ about some local and possibly slowly varying mean value $\overline{\theta}$ near the top of the planetary boundary layer can be expected to be predominantly generated by horizontal advection of air masses from warmer or colder regions. To simplify notation, we neglect zonal and temporal variations of the mean potential temperature $\overline{\theta}$ and focus on the dominant meridional variations, and we introduce the meridional distance coordinate $y = a\phi$ (Earth's radius $a$ and latitude $\phi$). Then, potential temperature anomalies $\theta'$ can be expanded in a Taylor series as (Corrsin 1974)

$$\theta'(y) \approx -\frac{\partial \overline{\theta}(y)}{\partial y}\eta + \frac{1}{2}\frac{\partial^2 \overline{\theta}(y)}{\partial y^2}\eta^2 + \cdots, \qquad (1)$$

where $\eta = y - y_0$ is a Lagrangian displacement of air masses arriving at $y$ from $y_0$; that is, $\eta$ is positive for a northward displacement and negative for a southward displacement. To the extent the first-order term dominates, a warm potential temperature anomaly $\theta' > 0$ in the Northern Hemisphere ($\partial_y \overline{\theta} < 0$) is generated by advecting warmer air masses from the south ($\eta > 0$), and a cold potential temperature anomaly $\theta' < 0$ is generated by advecting colder air masses from the north ($\eta < 0$)—in accordance with intuition and observed temperature variations (Screen 2014).

The first-order term dominates if the mean potential temperature varies on a length scale $\overline{L} = 2|\partial_y \overline{\theta}/\partial_{yy}\overline{\theta}|$ that is larger than the mixing length $L'$. The mixing length $L'$ is the characteristic distance over which meridional airmass displacements $\eta \sim L'$ transport properties such as potential temperature, before mixing with the environment (Corrsin 1974). It can be obtained from calculations of Lagrangian tracer trajectories as the product $L' = V\tau$ of the rms meridional velocity $V$ and the Lagrangian integral time scale $\tau$, which is the time scale

over which meridional velocities of air masses remain correlated (Taylor 1921; Bennett 1987). Indeed, $\overline{L} \gg L'$ is usually satisfied in Earth's atmosphere. The mean length scale $\overline{L}$ near the surface in midlatitudes is on the order of $10\,000\,\text{km}$ or greater in the zonal mean in all seasons. By contrast, the mixing length $L'$ near the surface is on the order of $900\,\text{km}$, given an rms meridional velocity $V \sim 10\,\text{m\,s}^{-1}$ and the measured Lagrangian integral time scale $\tau \sim 1$ day (Swanson and Pierrehumbert 1997; Daoud et al. 2003). Dividing synoptic potential temperature anomalies $\theta'$ near the surface by mean gradients $\partial_y \overline{\theta}$ also gives similar mixing lengths (Keppel-Aleks et al. 2011, 2012). So retaining only the first-order term in the expansion (1) is justifiable and is expected to lead to errors of about 10% in the zonal mean in midlatitudes, although regional errors may be greater.

That potential temperature variations on synoptic time scales are generated primarily by advection along a mean potential temperature gradient underlies the successful diffusive closures for near-surface potential temperature fluxes (Kushner and Held 1998), and is also supported by the observed strong correlation between potential temperature variations and variations of passive tracers such as carbon dioxide on synoptic time scales (Keppel-Aleks et al. 2011, 2012). It means that the synoptic potential temperature variance to first order scales like (Bennett 1987)

$$\overline{\theta'^2} \sim (\partial_y \overline{\theta})^2 L'^2, \tag{2}$$

a relation that has been used in scaling theories of quasigeostrophic turbulence (e.g., Held and Larichev 1996; Held 1999) and of atmospheric macroturbulence more generally (e.g., Schneider and Walker 2008). As usual for mixing length closures, variance–gradient relations like (2) can only be expected to hold on spatial scales larger than the length scales of the advecting eddies ($\gtrsim 1000\,\text{km}$) and on time scales longer than their equilibration time with the mean flow ($\gtrsim 20$ days). Changes $\Delta \overline{\theta'^2}$ in the synoptic potential temperature variance then scale with changes $\Delta(\partial_y \overline{\theta})^2$ in the squared potential temperature gradient and changes $L'^2$ in the squared mixing length:

$$\frac{\Delta \overline{\theta'^2}}{\overline{\theta'^2}} \sim \frac{\Delta(\partial_y \overline{\theta})^2}{(\partial_y \overline{\theta})^2} + \frac{\Delta L'^2}{L'^2}. \tag{3}$$

This implies that the variance $\overline{\theta'^2}$ diminishes as the meridional potential temperature gradient $|\partial_y \overline{\theta}|$ weakens under polar amplification of global warming, unless an increase of the mixing length $L'$ overcompensates the weakening of the gradient. Note that the Lagrangian mixing length $L'$ need not be equal to Eulerian eddy length scales. It generally is smaller, particularly near the surface, where strong thermal coupling to the surface

leads to Lagrangian integral time scales $\tau$ that are smaller (about 1 day) than eddy time scales (several days) (Swanson and Pierrehumbert 1997; Daoud et al. 2003).

### b. Changes under global warming

Global warming in comprehensive climate simulations typically is accompanied by an Arctic warming that is about a factor of 2–3 greater in the annual mean than the global- or tropical-mean warming (Holland and Bitz 2003; Collins et al. 2013). (Because the tropics cover about half of the globe but the Arctic only a comparatively small area, global- and tropical-mean warmings are similar.) This translates into a reduction of the Northern Hemisphere meridional potential temperature gradient $|\partial_y \overline{\theta}|$ of around 3%–7% for every kelvin of global-mean warming, given today's annual-mean near-surface potential temperature contrast between the tropics and the Arctic of approximately $30\,\text{K}$. There is considerable spread in the precise magnitude of Arctic amplification among models, and it depends on the season and vertical level that is considered (Holland and Bitz 2003; Screen et al. 2012; Collins et al. 2013). In the cold season, for example, the mean Arctic warming exceeds the global- or tropical-mean warming by more than a factor of 4 averaged across current climate models (Collins et al. 2013). The cold-season Arctic-to-equator potential temperature contrast near the surface is also greater ($\sim 45\,\text{K}$) but this still implies a larger reduction of the meridional potential temperature gradient ($\sim 7\%\,\text{K}^{-1}$ in the mean across models). For the sake of our argumentation here, however, the order of magnitude (3%–7%\,$\text{K}^{-1}$) of the expected gradient reduction suffices.

Relative changes of the mixing length are usually smaller. Let us first take an Eulerian perspective, as that is what was implicit in the studies cited in the introduction (Francis and Vavrus 2012; Liu et al. 2012). In the midlatitudes of Earth's atmosphere and of Earthlike atmospheres more generally, the meridional and zonal length scales of the energy-containing transient eddies are similar, and both are similar to the characteristic length scale of baroclinic instability (Boer and Shepherd 1983; Shepherd 1987; Schneider and Walker 2006; Merlis and Schneider 2009). A measure of that length scale is the effective Rossby radius (O'Gorman 2011):

$$L_R = \frac{N_{\text{eff}}^p \Delta_p}{f}, \tag{4}$$

a generalization of the traditional dry Rossby radius to moist atmospheres. The effective Rossby radius depends on an effective static stability measure $N_{\text{eff}}^p$ in pressure ($p$) coordinates, on the pressure difference $\Delta_p$

between the tropopause and the surface, and on the Coriolis parameter $f$. The effective static stability $N_{\text{eff}}^p$ is approximately the mean static stability that eddies experience in a moist atmosphere (O'Gorman 2011; Booth et al. 2015). It is smaller than the traditional dry static stability, because it takes into account the dynamic heating associated with latent heat release in saturated updrafts. The traditional dry Rossby radius generally increases under global warming, primarily because the tropopause height ($\Delta_p$) increases (Thuburn and Craig 2000; Schneider 2007; O'Gorman 2011), but also because the dry static stability increases as a result of increased latent heat release in a warmer atmosphere (Frierson 2008; Schneider and O'Gorman 2008). However, the effective Rossby radius and eddy length scale change little, because a decreasing effective static stability ($N_{\text{eff}}^p$) can partially compensate an increasing tropopause height ($\Delta_p$): over a wide range of climates simulated with an idealized GCM, including climates about 15 K warmer in the global mean than Earth's today, the effective Rossby radius and eddy length scale increase by only about 1% per kelvin global-mean warming (O'Gorman 2011). Comprehensive climate simulations exhibit a similarly weak increase of the eddy length scale under global warming (Kidston et al. 2010). So from an Eulerian perspective, one would not expect the scales of the energy-containing eddies to increase enough to drive a mixing length increase that overcompensates the 3%–7% K$^{-1}$ reduction of the meridional potential temperature gradient in its effect on the synoptic potential temperature variance.

Note that the effective Rossby radius (4) and thus the Eulerian eddy length scale do not depend in any simple and direct way on the meridional potential temperature gradient or the upper-level jet speed, as has been suggested (e.g., Francis and Vavrus 2012; Liu et al. 2012; Cohen et al. 2014). To the extent they do, through dependence of the effective static stability on the meridional potential temperature gradient, a reduction of the meridional potential temperature gradient triggered by polar amplification of global warming reduces (rather than increases) the effective static stability and the effective Rossby radius, because a less baroclinic atmosphere is statically effectively less stable (Schneider and Walker 2006; O'Gorman 2011). This is in part what compensates the effect of the increasing tropopause height on the eddy length scale.[1]

---

[1] A length scale that does depend directly on the mean zonal flow speed $\overline{u}$ is the stationary (barotropic) Rossby wave scale $L^* \sim (\overline{u}/\beta)^{1/2}$, where $\beta$ is the gradient of the Coriolis parameter $f$. This stationary-wave scale decreases with decreasing zonal flow speed and so likewise is not expected to drive increases in near-surface temperature variances. However, our focus here is on transient eddies.

From a Lagrangian perspective, the mixing length $L' = V\tau$ can increase through increases in the rms meridional velocity $V$ or the Lagrangian integral time scale $\tau$. Eddy kinetic energies under global warming in comprehensive climate simulations tend to increase in winter and decrease in summer in the Northern Hemisphere, and in the Southern Hemisphere they tend to increase throughout the year. However, the changes are weak: eddy kinetic energies change by approximately 2% per kelvin global-mean warming averaged across models (O'Gorman 2010). This implies weak changes in rms meridional velocity $V$, of approximately 1% per kelvin global-mean warming for isotropic eddy kinetic energy changes. So the Lagrangian integral time scale $\tau$, for example, in winter would have to increase by more than approximately 6% K$^{-1}$ to overcompensate the effect of the reduced meridional potential temperature gradient on the synoptic potential temperature variance. The integral time scale is controlled by the eddy turnover time and the thermal damping exerted on near-surface dynamics through boundary layer turbulence, which we do not expected to change drastically. Thus, it is difficult to see how such a large change of the integral time scale could arise.

To be sure, these are scaling arguments with considerable uncertainties. But they are rooted in the physics controlling synoptic potential temperature variations in midlatitudes. They suggest that we should expect a reduction of the synoptic potential temperature variance in the Northern Hemisphere as a result of Arctic amplification of global warming, unless other processes not considered here (e.g., land–atmosphere feedbacks and moist-convective processes) play a role. Potential temperature variations along near-surface isobars are proportional to temperature variations, so the same holds for temperature variations near the surface.

## 3. Observed distribution of temperature variations

The mean and variance of the potential temperature distribution only determine the frequency of extremes if the PDF is Gaussian. Otherwise, higher moments of the distribution must also be considered. The PDF of potential temperature variations can be expected to be Gaussian, or nearly so, under a variety of circumstances. For example, potential temperature variations $\theta'$ depend linearly on the displacement $\eta$ if the expansion of potential temperature variations (1) holds with only the first-order term in $\eta$ and if the meridional potential temperature gradient $\partial_y \overline{\theta}$ that eddies "see" is fixed in time (rather than being strongly modified by the eddies themselves). In this case, mixing is weak, and if the statistics of airmass displacements $\eta$ are Gaussian,
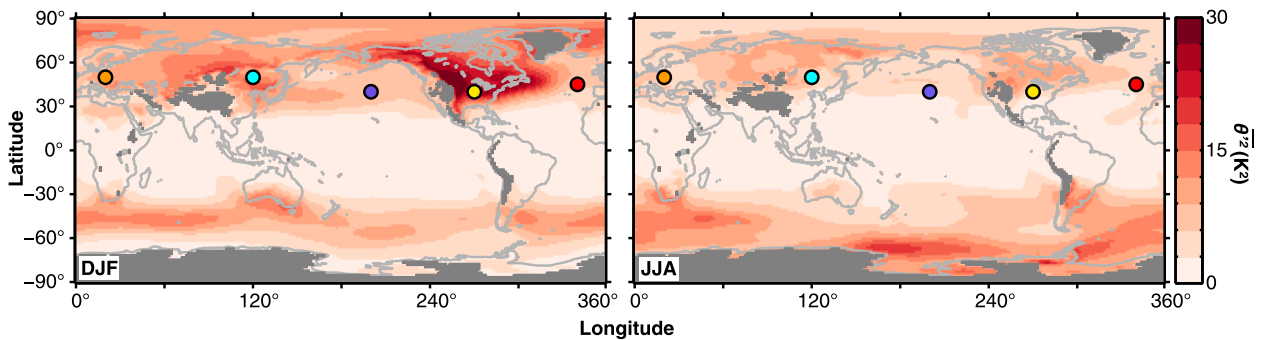
FIG. 1. Climatological variance of synoptic 850-hPa potential temperature variations for (left) DJF and (right) JJA. The potential temperature variations are from ERA-Interim data for 1980–2010 (Dee et al. 2011) and were bandpass filtered to 3–15-day time scales. In the gray regions, topography extends above the mean 850-hPa isobar. (The colored circles mark the locations for which the PDFs of the potential temperature variations are shown in Fig. 2, with the color of the circles corresponding to the line colors in Fig. 2.)

potential temperature variations $\theta'$ will inherit their Gaussian statistics. On the other hand, departures from Gaussianity can arise in several ways and are common in turbulent flows. For example, if higher-order terms involving higher derivatives of the mean potential temperature need to be considered in the expansion (1), non-Gaussian statistics can arise through the terms that are nonlinear in $\eta$ (Kimura and Kraichnan 1993). Or PDFs with a Gaussian core but exponential ("fat") tails for fluctuations larger than about a standard deviation commonly arise when air masses occasionally undergo Lagrangian displacements over distances that are unusually large relative to what is expected under Gaussian statistics, without equilibrating and losing the memory of their initial potential temperature (Pumir et al. 1991; Shraiman and Siggia 1994, 2000; Warhaft 2000; Pierrehumbert 2000). In that case, mixing is strong, and large potential temperature deviations from the mean occur more frequently than the variance alone would suggest under Gaussian statistics. An earlier examination of near-surface potential temperature variations in reanalysis data gave no indication that such strong mixing and non-Gaussian PDFs occur (Swanson and Pierrehumbert 1997), presumably because potential temperature in the mean varies on scales much larger than the mixing length, and near-surface air temperatures are strongly forced by the lower boundary. However, recent examinations of surface temperature variations that were not restricted to synoptic time scales but included longer time scales found significant departures from Gaussian statistics (e.g., Ruff and Neelin 2012; Huybers et al. 2014; Loikith et al. 2015).

Here, we reexamine synoptic potential temperature variations in the modern ERA-Interim atmospheric reanalysis produced by the European Centre for Medium-Range Weather Forecasts (Dee et al. 2011). We consider 850-hPa potential temperature variations

for the December–February (DJF) and June–August (JJA) seasons for the years 1980–2010, bandpass filtered to 3–15-day time scales. Figure 1 shows the climatological variance of these filtered potential temperature variations for the two seasons. The enhanced variance in the winter hemisphere, especially over continents and in the storm track regions, is clearly evident. We used a kernel density estimator to obtain PDFs of the synoptic potential temperature variations, and we constructed pointwise 95% confidence intervals for the estimated PDFs using a bootstrap procedure (see appendix A).

Figure 2 shows the estimated PDFs and 95% confidence intervals for the midlatitude locations that are marked by circles in Fig. 1. The locations cover continents and the oceanic storm track regions and are representative of midlatitudes generally. (We have verified that our conclusions in what follows hold generally at locations throughout the midlatitudes.) At all locations and in both seasons, the estimated PDFs are statistically indistinguishable from Gaussian. The raw PDFs show the different mean values and variances of potential temperature variations at the different locations in the two seasons (Fig. 2, top). Once the PDFs are standardized by subtracting the mean and dividing by the standard deviation for each location and season, it is evident that the cores of the PDFs are nearly Gaussian: the estimated 95% confidence intervals (color shading) generally include the standard normal distribution (Fig. 2, middle). Plotting the estimated PDFs with a logarithmic axis, so that the standard normal distribution becomes a parabola, makes any departures from Gaussianity in the tails of the distributions clearer (Fig. 2, bottom). Out to three standard deviations, which are exceeded only 0.3% of the time for a Gaussian random variable, the estimated PDFs and confidence intervals enclose the standard normal
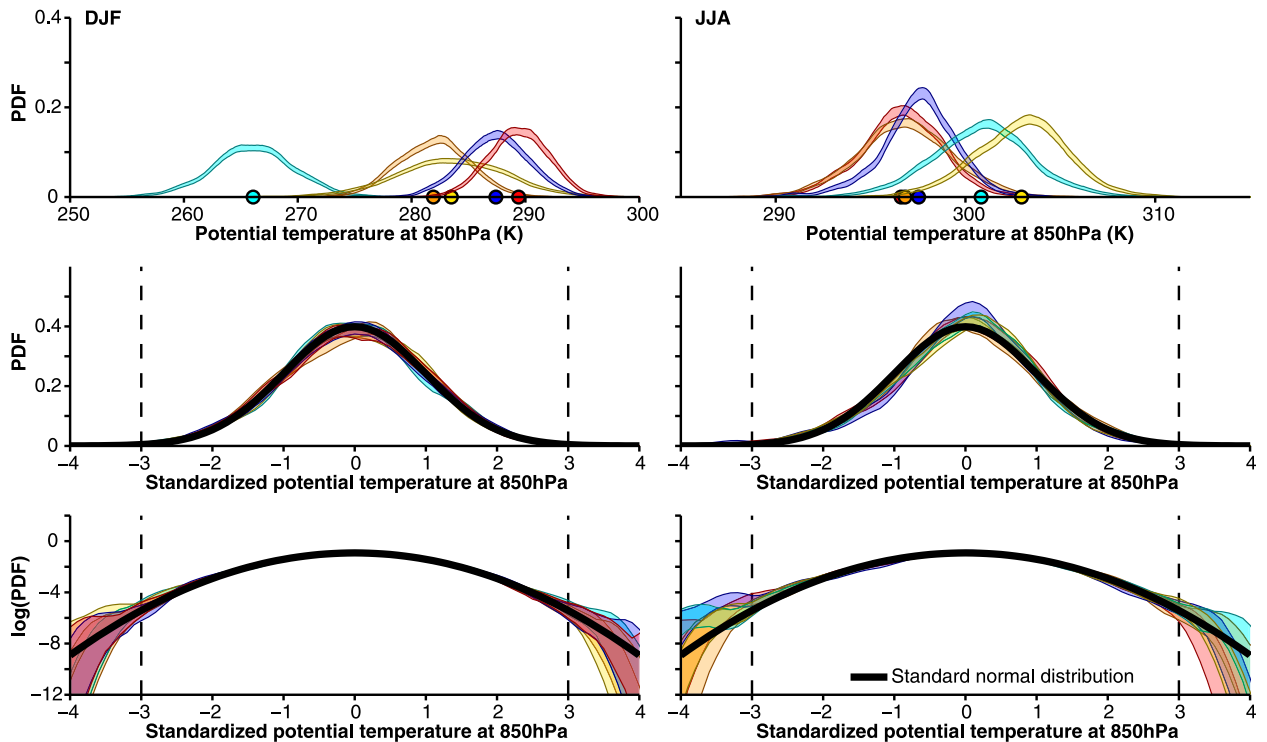
FIG. 2. Estimated PDFs of synoptic 850-hPa potential temperature variations at the five representative midlatitude locations marked in Fig. 1, for (left) DJF and (right) JJA. The locations are in the Pacific storm track (40°N, 160°W; purple), Atlantic storm track (45°N, 20°W; red), central Europe (50°N, 20°E; orange), northern China (50°N, 120°E; light blue), and midwestern United States (40°N, 90°W; yellow). (top) Raw PDFs, with circles on the potential temperature axes marking mean values. (middle) PDFs standardized with the mean and standard deviation for each location and each season. (bottom) As in the middle row, but with a logarithmic axis for the PDF. Color shading indicates pointwise 95% confidence intervals estimated by a bootstrap procedure (appendix A). Black lines show the standard normal distribution, and dashed lines indicate three standard deviations. The PDFs are estimated from the same filtered potential temperature variations whose variance is shown in Fig. 1.

distribution tightly. Larger deviations from the mean are very rare, and the sampling error in estimating PDFs becomes relatively large. But the estimated PDFs remain statistically indistinguishable from Gaussian. There are hints, especially in JJA, of sub-Gaussian behavior in the tails, which intimates that large potential temperature deviations may occur less frequently than the variance alone would suggest under Gaussian statistics. However, the departures from Gaussianity are not statistically significant according to a Kolmogorov–Smirnov test ($p$ values exceed 0.05), except in the Pacific storm track in JJA (purple curve in Fig. 2). We have verified that PDFs for bandpass-filtered surface air temperature variations also have Gaussian shapes to a similar degree as the 850-hPa potential temperature variations, at least out to three standard deviations; in the tails beyond three standard deviations, the estimated surface-temperature PDFs in some locations (e.g., over the Pacific Ocean in DJF) depart slightly from Gaussianity, but not in a manner that is clearly statistically significant in all locations.

This analysis suggests that for understanding how the frequency of even rare and large synoptic potential temperature variations changes with climate, at least for now it suffices to understand changes in the mean and variance of the PDFs. Changes owing to modifications of higher moments may not be identifiable, given that departures from Gaussianity are not clearly identifiable in reanalysis data for the present climate. This does not preclude the possibility that on other than synoptic time scales, when processes and feedbacks other than advection play a larger role, higher moments are more important. For example, land–atmosphere feedbacks may become important on longer time scales (e.g., Schär et al. 2004; Seneviratne et al. 2006, 2010; Berg et al. 2014). They and other feedback processes may account for the non-Gaussian tails of PDFs commonly seen when temperature variations with longer time scales are included (e.g., Ruff and Neelin 2012; Huybers et al. 2014; Loikith et al. 2015). Indeed, when potential temperature variations are not filtered, so that lower-frequency variations remain included, or if they are filtered to time

scales longer than approximately 25 days, departures from Gaussianity become significant: PDFs of such lower-frequency variations often have sub-Gaussian tails (see appendix A for an example). This indicates that nonlinear processes must be operating on such time scales. Where they generate sub-Gaussian tails, such nonlinear processes damp large deviations relative to normal statistics. While much of the literature so far has focused on amplifying feedbacks, the data suggest damping feedbacks also play a role on longer time scales in the climatology. However, here we continue to focus on synoptic time scales.

## 4. Idealized GCM simulations

We test the validity of the theoretical arguments and changes in the PDF of near-surface potential temperatures more quantitatively in simulations with an idealized GCM, which has a hydrologic cycle, an entirely water-covered surface, and a simple representation of ocean heat transport in low latitudes (O'Gorman and Schneider 2008b; Levine and Schneider 2011). This aquaplanet setting allows us to abstract, for the moment, from the added complications of continentality, land–atmosphere feedbacks, etc. To explore whether synoptic transient eddies amplify as the climate warms through more frequent resonances in stationary waveguides, as was suggested by Petoukhov et al. (2013), we added in the Northern Hemisphere a Gaussian mountain that is 4 km high, is centered at 45°N, and has a standard width of 15° in longitude, to excite orographic stationary waves with zonal wavenumbers 6–8. This is a water-mountain; that is, the surface properties of the mountain are equal to those of the surrounding water surface. The Southern Hemisphere remains without topography. See appendix B for details of the model setup.

With the idealized GCM at a relatively high resolution (spectral T127 resolution in the horizontal and 30 vertical levels), we simulated six climates in statistically steady states by rescaling the longwave optical thickness of the atmosphere (O'Gorman and Schneider 2008b). The climates span a wide range of surface temperatures, from very cold (global-mean surface temperature of 273 K, pole-to-equator contrast of 45 K) to very warm (global-mean surface temperature of 310 K, pole-to-equator contrast of 23 K). In between lies an Earthlike reference climate, with a global-mean surface temperature of 289 K, and with a pole-to-equator surface temperature contrast of 35 K that is representative of a winter hemisphere on present-day Earth. The idealized GCM simulations exhibit polar amplification of global warming, although, for example, there is no ice-albedo feedback, in part because the poleward latent

and total energy transports strengthen as the climate warms in these simulations (O'Gorman and Schneider 2008b; Schneider et al. 2010). The polar warming is greater than the global-mean warming by a factor that ranges from 1.4 in the coldest simulation to 1.8 in the warmest simulation. This amplification factor is lower than that in comprehensive climate models because of the missing feedback processes (Holland and Bitz 2003; Masson-Delmotte et al. 2013). But the range of climates and hence of pole-to-equator surface temperature contrasts we simulated is much larger than that typically considered (e.g., the pole-to-equator temperature contrast changes by a factor of 2 in our simulations). So changes in the PDF and in extremes of near-surface temperatures or potential temperatures that are caused by changes in meridional temperature gradients should be readily evident. Additionally, this idealized GCM, like other, even further idealized GCMs (e.g., Mbengue and Schneider 2013), exhibits atmospheric circulation changes similar to those commonly seen in more comprehensive models. For example, the Hadley circulation widens, storm tracks shift poleward, and the eddy kinetic energy changes weakly as the climate warms (O'Gorman and Schneider 2008a; Schneider et al. 2010; Levine and Schneider 2011). This demonstrates that additional feedback mechanisms, for example, associated with clouds, are not necessary to obtain such circulation changes. It also means that if such circulation changes modify the distribution of near-surface temperatures or potential temperatures, as has been suggested (Cohen et al. 2014), their effect should be apparent in our simulations. As before, we focus on synoptic potential temperature variations, bandpass filtered to time scales of 3–15 days (see appendix A), here at the $\sigma = 0.85$ coordinate level of the GCM, where $\sigma = p/p_s$ is the pressure $p$ normalized by the surface pressure $p_s$ (i.e., the level $\sigma = 0.85$ has a mean pressure of 850 hPa, except over the mountain).

Figure 3 illustrates for two sample climates that, as the climate warms in the simulations, the tropopause rises (Fig. 3a)—essentially for radiative balance reasons (see, e.g., Schneider 2007). Meridional potential temperature gradients near the surface weaken (Fig. 3b). The speed of the upper-level jets, at a fixed latitude and level (e.g., 45° latitude and 500 hPa), decreases, in accordance with thermal wind balance in pressure coordinates,

$$\frac{\partial \overline{u}}{\partial p} = \frac{R}{fp}\left(\frac{p}{p_0}\right)^{\kappa}\left(\frac{\partial \overline{\theta}}{\partial y}\right)_p, \quad (5)$$

with zonal wind $u$, reference pressure $p_0$, gas constant of air $R$, adiabatic exponent $\kappa = R/c_p$, and specific heat at constant pressure $c_p$. However, because the tropopause
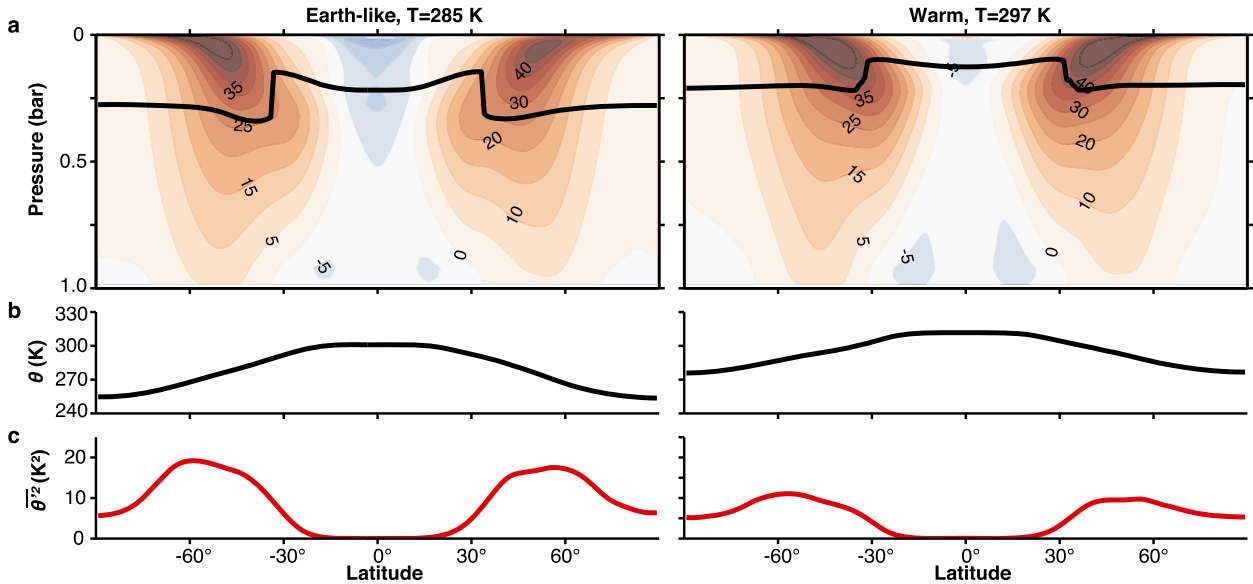
FIG. 3. Zonal- and temporal-mean statistics of two sample climates simulated with the idealized GCM. (left) An Earthlike climate, with a global-mean surface temperature of 285 K, and (right) a warm climate, with a global-mean surface temperature of 297 K. (a) Zonal wind (color contours, m s$^{-1}$) and tropopause (black line, identified as a 2 K km$^{-1}$ isoline of the temperature lapse rate). The fields are interpolated from the model's $\sigma$ coordinates to pressure coordinates for plotting. (b) Potential temperature at the $\sigma = 0.85$ level. (c) Synoptic potential temperature variance at $\sigma = 0.85$, bandpass filtered to 3–15-day time scales.

rises, so that the layer deepens over which the thermal wind balance (5) must be integrated to obtain the jet speed just below the tropopause, the upper-tropospheric jet speeds can actually increase, despite the reduction of meridional potential temperature gradients near the surface (e.g., see the jet speeds near the tropopause in Fig. 3a). Additionally, it is evident that the widening of the Hadley circulation and other circulation changes also modify the meridional structure of the jets, particularly in the upper troposphere. However, as a result of the reduced meridional potential temperature gradient (Fig. 3b), the near-surface synoptic potential temperature variance decreases in both hemispheres, with and without the mountain (Fig. 3c). This is consistent with what is seen in other idealized GCM simulations (Schneider and Walker 2008; Hassanzadeh et al. 2014).

### a. Potential temperature variance

Figure 4a shows how the near-surface synoptic potential temperature variance $\overline{\theta'^2}$ in midlatitudes varies across the spectrum of simulations, each identified by its global-mean surface temperature. The variance here is the bandpass-filtered transient potential temperature variance at the $\sigma = 0.85$ level; that is, it does not include the spatial variance owing to stationary eddies generated by the mountain in the Northern Hemisphere. It is evident that this variance generally decreases as the climate warms, both in the hemisphere with the mountain and in the hemisphere without topography. The

variance decreases by about 4.5% per kelvin global-mean warming as the climate warms from the Earthlike mean temperature of 289 K to the hothouse mean temperature of 300 K. Almost all (90%) of that variance reduction can be accounted for by the reduction of the meridional potential temperature gradient that arises because the global warming is amplified near the poles: The squared potential temperature gradient $(\partial_y \overline{\theta})^2$ decreases by 4.1% per kelvin global-mean warming as the climate warms from 289 to 300 K (Fig. 4b).

The remainder of the variance changes can be attributed to changes in a squared mixing length $L'^2 = \overline{\theta'^2}/(\partial_y \overline{\theta})^2$, which is the mixing length implied by the variance and meridional potential temperature gradient if one assumes (2) is satisfied. That is, here we take $L'$ not to be an independently determined Lagrangian mixing length, which would have to be obtained from Lagrangian tracer trajectory calculations; because of limited data availability, it would be difficult to carry them out for the comprehensive climate models we will discuss below. Instead, we determine the implied mixing length $L'$ as a residual that accounts for all variance changes that cannot be attributed to gradient changes, irrespective of their physical origin. This suffices for our purposes as long as this residual does not become dominant. Indeed, in the simulations, the implied $L'^2$ does not vary monotonically but changes by less than 0.7% per kelvin global-mean warming, except for a larger change toward the warmest simulation (Fig. 4c).
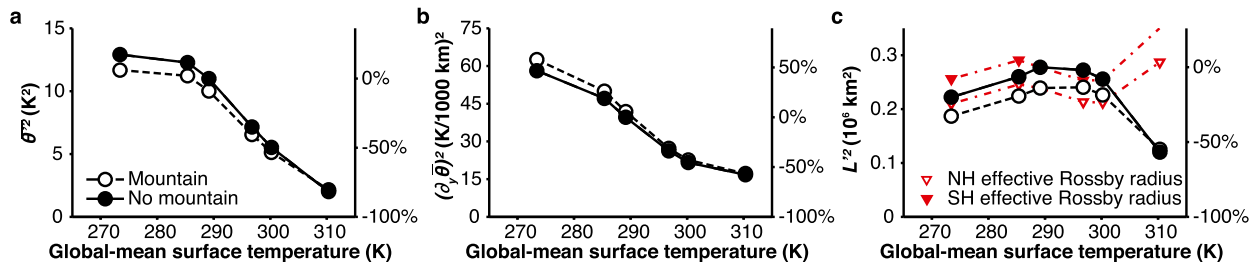
FIG. 4. Synoptic near-surface potential temperature variance, mean potential temperature gradient, and mixing length in idealized GCM simulations. (a) Synoptic potential temperature variance $\overline{\theta'^2}$ at the $\sigma = 0.85$ level, bandpass filtered to 3–15-day time scales and averaged between 20° and 70° latitude in each hemisphere. (b) Squared potential temperature gradient $(\partial_y \overline{\theta})^2$ at the same level, evaluated from the mean potential temperature difference between 20° and 70° latitude in each hemisphere. (c) Squared mixing length (circles) $L'^2 = \overline{\theta'^2}/(\partial_y \overline{\theta})^2$ implied by the variance in (a) and the gradient in (b). Red triangles indicate the effective Rossby radius (4), evaluated as in O'Gorman (2011) and likewise averaged between 20° and 70° latitude in each hemisphere, with a scaling constant chosen so that the effective Rossby radius matches the mixing length in the Northern Hemisphere for the simulation with a global-mean surface temperature of 289 K. Each simulation is identified by its global-mean surface temperature on the horizontal axes. The right vertical axes give the percentage changes of each quantity relative to the Southern Hemisphere in the Earthlike simulation with a global-mean surface temperature of 289 K. Open symbols are for the Northern Hemisphere with a Gaussian mountain; closed symbols are for the Southern Hemisphere without topography.

Variations of the effective Rossby radius (4) are similarly small (Fig. 4c, red triangles). Only the warmest simulation, with a hothouse global-mean surface temperature of 310 K, deviates from this pattern in that a decreasing mixing length is also important to account for the variance reduction in that simulation, and the effective Rossby radius does not capture this decrease. This is a climate in which the extratropics are strongly convective, and near-surface potential temperature variations are weak (Schneider and O'Gorman 2008). It appears that moist-convective damping of eddies in this climate may lead to a substantial reduction of the Lagrangian mixing length, while Eulerian eddy length scales change much less.

In these simulations, the hemisphere with the mountain does not appear to behave in any substantially different way than the hemisphere without topography. That is, while the presence of the mountain introduces stationary waves, it does not change the result that the synoptic variance decreases as the climate warms, and that almost all of the variance reduction can be accounted for by the reduction of the meridional potential temperature gradient. It is possible that with different topographic configurations, resonances in stationary waveguides would modify transient eddies. But the simulations show that such resonant modification is not generally to be expected under global warming.

The reduction of the synoptic potential temperature variance near the surface and its attribution primarily to the reduction of the meridional potential temperature gradient is consistent with the scaling arguments in section 2. It implies a reduced frequency of cold outbreaks, both because the mean of the (potential) temperature distribution shifts toward higher temperatures and the variance decreases—unless there are nonnormal changes in higher moments of the distribution.

### b. Probability density functions

Figure 5 shows the PDFs of synoptic potential temperature variations at 45°N and 45°S, which is representative of the midlatitudes more generally. The PDFs are statistically indistinguishable from Gaussian at least out to three standard deviations, both at 45°S (no mountain; Fig. 5, left) and at 45°N/90°E, downstream of the mountain (Fig. 5, right). (How far downstream of the mountain the PDFs are estimated does not affect our results.) Changes in the probability of potential temperature variations at least out to three standard deviations can be accounted for by changes in the mean and variance, with mean shifts dominating the changes in the distribution. Beyond three standard deviations, there is a hint that tails of the PDFs evolve from sub-Gaussian to super-Gaussian as the climate warms; however, the significance of the departures from Gaussianity in the tails is unclear. There is no evidence that resonances in stationary waveguides amplify synoptic potential temperature variations in the hemisphere with the mountain as the climate warms: the PDF changes in the hemisphere with the mountain and in the hemisphere without a mountain are not statistically distinguishable. This may be because specific circulation conditions that would favor such resonances (e.g., split extratropical jets; see Petoukhov et al. 2013; Coumou et al. 2014) do not occur with increased frequency as the climate warms in our specific idealized GCM. But at the
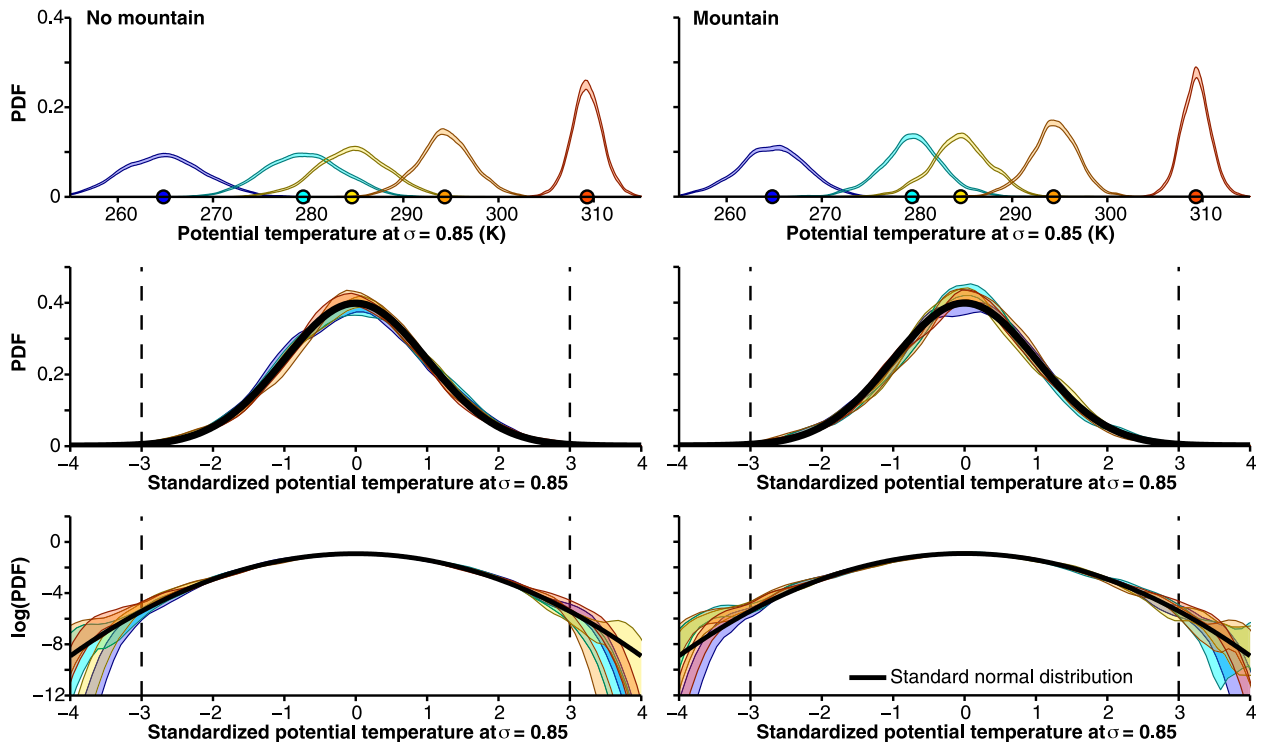
FIG. 5. Estimated PDFs of synoptic near-surface potential temperature variations at 45°N and 45°S in the idealized GCM simulations. Potential temperature variations are evaluated at $\sigma = 0.85$ and are bandpass filtered to 3–15-day time scales for (left) Southern Hemisphere (without topography) and (right) Northern Hemisphere (with mountain). (top) Raw PDFs, with circles on the potential temperature axes marking the mean values. (middle) PDFs standardized with the mean and standard deviation for each location and each simulation. (bottom) As in the middle row, but with a logarithmic axis for the PDF. Color shading indicates pointwise 95% confidence intervals, as in Fig. 2, estimated by a bootstrap procedure (appendix A). Black lines show the standard normal distribution, and dashed lines indicate three standard deviations.

very least, our results show that favoring of such resonances is not generally to be expected under global warming, consistent with the observational findings of Screen and Simmonds (2013a).

The results from the idealized GCM demonstrate that the theoretical arguments can account for changes in synoptic potential temperature variations near the surface. The simulations provide a test of the arguments in a setting unencumbered by processes that may lead to more complex behavior, such as land–atmosphere feedbacks. They may be expected to carry over at least to ocean regions on Earth.

## 5. Comprehensive climate simulations

To examine the extent to which the results discussed so far carry over to more realistic situations, we examine near-surface potential temperature variations and their changes under global warming in an ensemble of comprehensive climate models that participated in phase 5 of the Coupled Model Intercomparison Project (CMIP5;

Taylor et al. 2012). We consider both historical simulations for the years 1980–99 and global warming simulations for the years 2080–99 under the representative concentration pathway 8.5 (RCP8.5) emission scenario, a scenario of comparatively high greenhouse gas emissions through the twenty-first century (Riahi et al. 2011). We again analyze synoptic potential temperature variations at 850 hPa, bandpass filtered to 3–15-day time scales. We screened the models by comparing their synoptic potential temperature variances in the historical simulations with the ERA-Interim variances at the five locations marked in Fig. 1, both in DJF and JJA. (Potential temperatures in the models were linearly interpolated to the same locations as in Fig. 1 for models for which the locations did not coincide with a grid point.) For what follows, we selected the 10 models for which the synoptic potential temperature variances are closest to the reanalysis variances in a least squares sense. According to this simple metric, this represents the top 50% of the models in the total CMIP5 ensemble for which daily temperatures are available, not counting

TABLE 1. Ensemble of CMIP5 models used in this study.

| Modeling center | Model name |
| --- | --- |
| Commonwealth Scientific and Industrial Research Organisation (CSIRO) and Bureau of Meteorology (BOM), Australia | ACCESS1.0 and ACCESS1.3 |
| Centro Euro-Mediterraneo per I Cambiamenti Climatici | CMCC-CM |
| Centre National de Recherches Météorologiques/Centre Européen de Recherche et Formation Avancée en Calcul Scientifique | CNRM-CM5 |
| Canadian Centre for Climate Modelling and Analysis | CanESM2 |
| NOAA/Geophysical Fluid Dynamics Laboratory | GFDL-CM3 and GFDL-ESM2M |
| Met Office Hadley Centre | HadGEM2-CC |
| L'Institut Pierre-Simon Laplace | IPSL-CM5A-MR |
| Japan Agency for Marine–Earth Science and Technology, Atmosphere and Ocean Research Institute (University of Tokyo), and National Institute for Environmental Studies | MIROC5 |

multiple ensemble members generated by individual models. The models included in our ensemble are listed in Table 1. (Our results are insensitive to this screening.) The model whose simulated variances are closest to the reanalysis is the HadGEM2-CC model.

### a. Potential temperature variance

Figure 6a shows the multimodel median of the synoptic potential temperature variance $\overline{\theta'^2}$ in the historical simulations for the DJF and JJA seasons of 1980–99. The spatial pattern and magnitude of the variance generally compares well with the observations (Fig. 1). For example, the enhanced variance in the winter hemisphere, especially over continents and in storm track regions, is clearly evident. Figure 6b shows the multimodel median of the percentage by which this variance changes in the RCP8.5 simulations relative to the historical simulations. In the Northern Hemisphere in winter, the variance generally decreases in middle and higher latitudes (by 25% in midlatitudes and more in higher latitudes, or by $\gtrsim$ 5% per kelvin global warming, given that the multimodel median DJF warming is 4.6 K). This is in agreement with the theoretical expectations of what effects the strong wintertime Arctic amplification should have (section 2). It is also in agreement with other modeling studies (Kitoh and Mukano 2009; Ylhäisi and Räisänen 2014; Screen et al. 2015) and with observations covering the past decades (Screen 2014). The variance also generally decreases in Northern Hemisphere midlatitudes in summer, especially over oceans, albeit less strongly than in winter. However, in summer there are also regions in which the variance increases, for example, over central and eastern Europe (Gregory and Mitchell 1995; Schär et al. 2004; Seneviratne et al. 2006), and around the Arctic Ocean, likely related to summer sea ice retreat (Collins et al. 2013). In the Southern Hemisphere, the variance decreases in winter (JJA) over the

Southern Ocean near Antarctica, but it increases over most of the Southern Ocean in summer (DJF). (Variance changes in the tropics and subtropics are more complex and are shaped by the distribution of continents and deep convection; however, they are not our focus here.)

Much of the spatial and seasonal structure of the synoptic variance changes can be accounted for by changes in the meridional potential temperature gradient $\partial_y\overline{\theta}$.[2] To obtain gradients on the scales of the energy-containing eddies in the atmosphere (on scales the eddies "see"), we smoothed the mean potential temperature with a spherical harmonics filter that gradually damped total (spherical) wavenumbers greater than 6 and completely filtered out wavenumbers greater than 10. Figure 6c shows the multimodel median of the percentage by which the so-obtained squared meridional potential temperature gradient $(\partial_y\overline{\theta})^2$ changes in the RCP8.5 simulations relative to the historical simulations. In the Northern Hemisphere in winter, the squared gradient $(\partial_y\overline{\theta})^2$ in middle and higher latitudes decreases, with a similar magnitude and spatial structure as the variance reduction (cf. Fig. 6b). In the Northern Hemisphere in summer, the squared gradient decreases over oceans, as does the variance, but the decrease of $(\partial_y\overline{\theta})^2$ is larger than that of the variance. In other regions, the squared gradient increases, for example, over central and eastern Europe and around the Arctic Ocean, where also the variance increases, again with

---

[2] Given that zonal potential temperature gradients in some regions are also large (e.g., near continental boundaries; see de Vries et al. 2012), one might also consider the total horizontal potential temperature gradient $\mathbf{V}_h\overline{\theta}$ and its changes under global warming. However, considering the total gradient $\mathbf{V}_h\overline{\theta}$ in place of the meridional gradient $\partial_y\overline{\theta}$ only modifies details of regional changes (e.g., the region of gradient increases over the Arctic Ocean in DJF; see Fig. 6c), but overall it does not materially change our results.
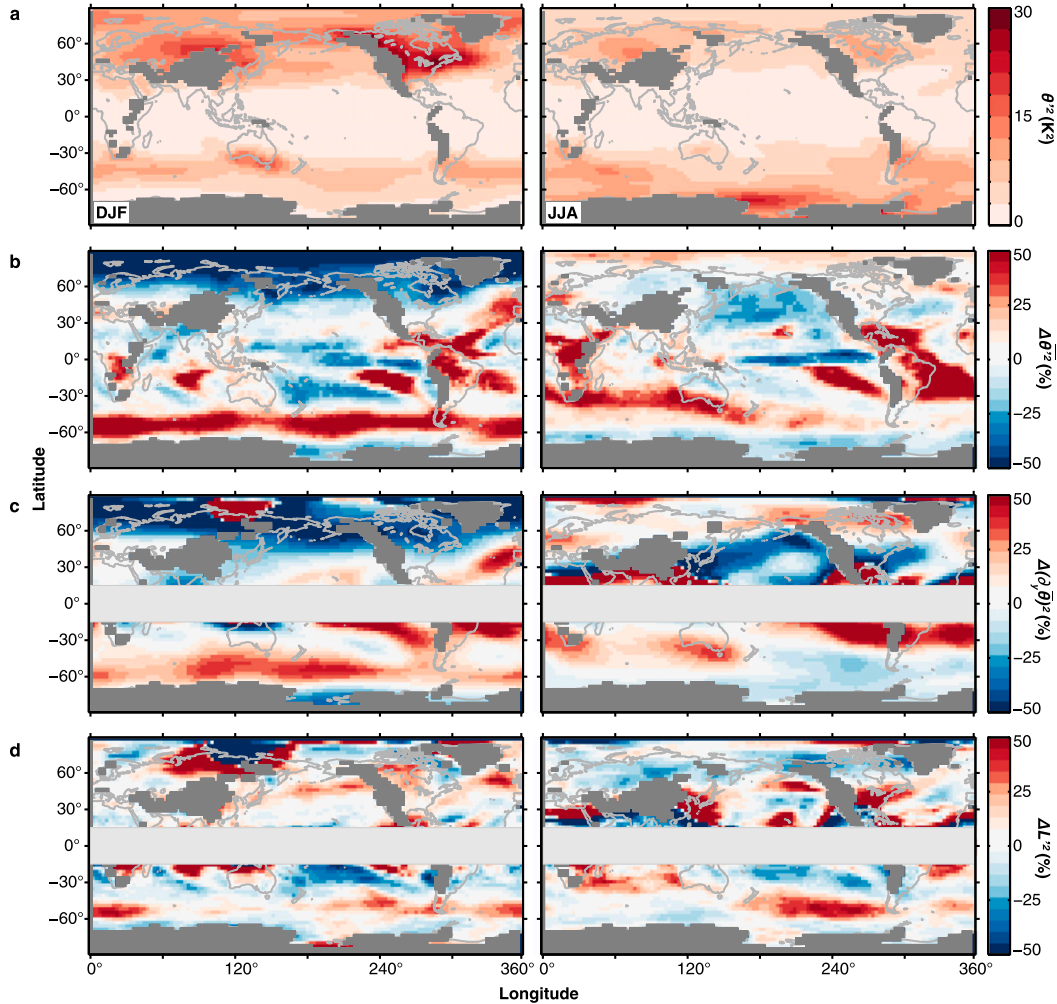
FIG. 6. CMIP5 multimodel median values of 850-hPa potential temperature statistics for (left) DJF and (right) JJA. (a) Synoptic potential temperature variance $\overline{\theta'^2}$ for the years 1980–99 of the historical simulations. (b) Percentage change of the synoptic potential temperature variance $\overline{\theta'^2}$ in the years 2080–99 of the RCP8.5 simulations relative to the years 1980–99 of the historical simulations shown in (a). (c) Percentage change of the squared meridional potential temperature gradient $(\partial_y \overline{\theta})^2$ in the years 2080–99 of the RCP8.5 simulations relative to the years 1980–99 of the historical simulations. (To calculate the gradients, mean potential temperatures were smoothed with a spherical harmonics filter that damped spherical wavenumbers greater than 6 and completely filtered out wavenumbers greater than 10.) (d) Percentage change of the squared mixing length $L'^2 = \overline{\theta'^2}/(\partial_y \overline{\theta})^2$ implied by the variance and meridional potential temperature gradient, in the years 2080–99 of the RCP8.5 simulations relative to the years 1980–99 of the historical simulations. Synoptic potential temperature variations are bandpass filtered to 3–15 days. In the dark gray regions, topography extends above the mean 850-hPa isobar. The light gray bar blocks out the equatorial region, where potential temperature gradients are weak and their percentage changes become large.

a similar magnitude of changes in both quantities. In the Southern Hemisphere, the seasonally varying changes in the squared gradient capture much of the spatial and seasonal pattern of variance changes over the Southern Ocean, primarily with increases in summer (DJF) and a mixture of increases and decreases in winter (JJA). Overall, the similarities of the pattern of changes in the variance $\overline{\theta'^2}$ (Fig. 6b) and in the squared gradient $(\partial_y \overline{\theta})^2$ (Fig. 6c) suggest that a large fraction of the $\overline{\theta'^2}$ changes

can be accounted for by $(\partial_y \overline{\theta})^2$ changes, especially in winter, without it being necessary to invoke feedback processes other than those that shape the mean potential temperature distribution. Indeed, the correlation coefficient between changes in $\overline{\theta'^2}$ and in $(\partial_y \overline{\theta})^2$ area averaged between 30° and 60° latitude is approximately 0.9 in winter (DJF in the Northern Hemisphere and JJA in the Southern Hemisphere), and approximately 0.3 in summer.
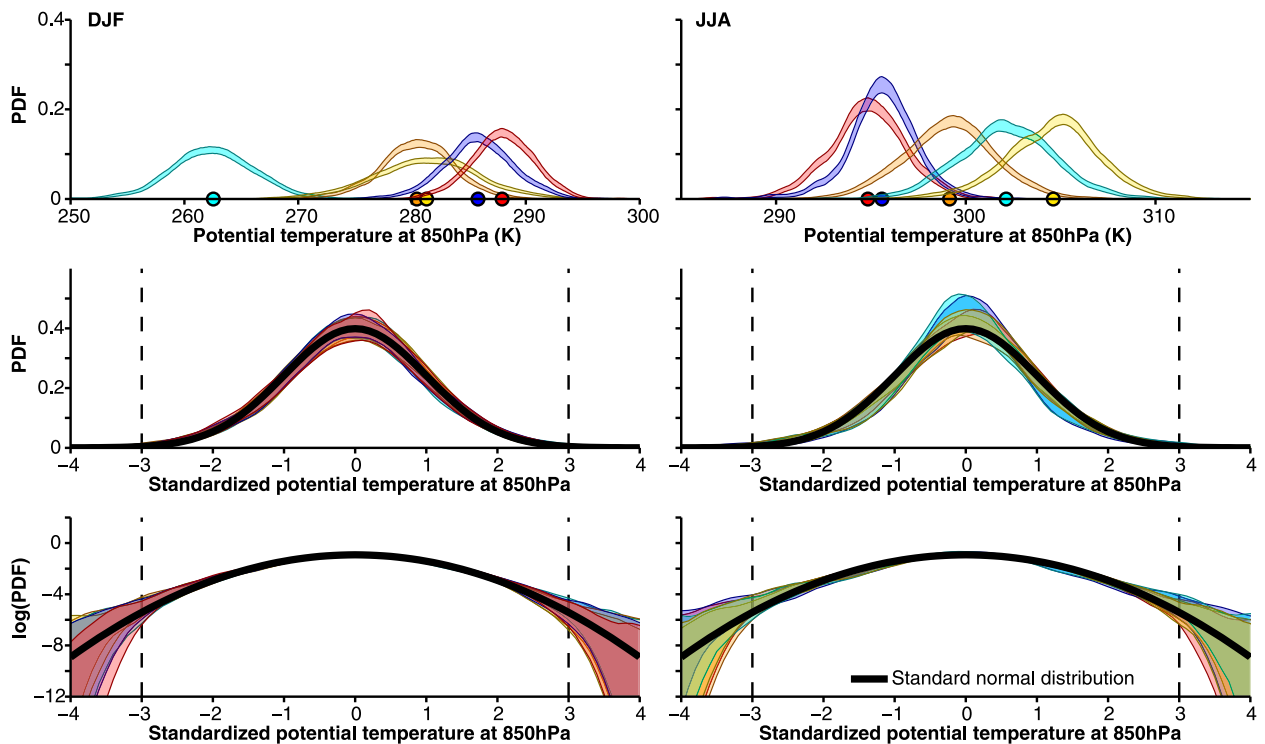
FIG. 7. Estimated PDFs of synoptic 850-hPa potential temperature variations in historical CMIP5 simulations for 1980–99, at the five representative midlatitude locations in Fig. 1, for (left) DJF and (right) JJA. Color coding of locations, bandpass filtering, and plotting conventions is as in Fig. 2. (top) Raw PDFs for the Hadley Centre model HadGEM2-CC. (middle) PDFs for all models in our ensemble, standardized with the mean and standard deviation for each location, season, and model. (bottom) As in the middle row, but with a logarithmic axis for the PDF. Color shading indicates pointwise 95% confidence intervals estimated by a bootstrap procedure (appendix A). Black lines show the standard normal distribution, and dashed lines indicate three standard deviations.

The remainder of the variance changes not accounted for by gradient changes can be attributed to changes in the squared mixing length $L'^2 = \overline{\theta'^2}/(\partial_y\overline{\theta})^2$ that is implied by the variance and meridional potential temperature gradient. Figure 6d shows the multimodel median of the percentage by which $L'^2$ changes. It is clear that $L'^2$ changes also play a role in determining variance changes, for example, in parts of the Southern Ocean. But overall, $L'^2$ changes are less coherent spatially and less clearly related to variance changes than the squared gradient changes. The correlation coefficient between changes in $\overline{\theta'^2}$ and in $L'^2$ area averaged between 30° and 60° latitude is approximately 0.7 in winter in either hemisphere, 0.2 in summer in the Northern Hemisphere, and 0.7 in summer in the Southern Hemisphere. The changes in the implied mixing length may reflect changes in actual mixing length as well as processes other than advection (e.g., land–atmosphere interactions) that modify the potential temperature variance. Unlike in the idealized GCM simulations, implied mixing length changes are not ignorable in accounting for variance changes in the comprehensive

climate simulations. Yet the gradient changes continue to dominate.

### b. Probability density functions

It remains to examine to what extent the mean and variance can account for the distribution of synoptic potential temperature variations in the historical and global-warming simulations. Do significant departures from Gaussianity exist in the simulations of the present climate or arise under global warming?

Figure 7 shows PDFs of synoptic potential temperature variations in the historical simulations at the same five locations marked in Fig. 1 for which the reanalysis PDFs were shown in Fig. 2. The raw PDFs estimated from one model—the Hadley Centre's HadGEM2-CC (see Table 1), whose synoptic variances were closest to the reanalysis—illustrate the spread of PDFs at the different locations and the two seasons. The PDFs from the Hadley Centre model are similar to those obtained from the reanalysis, with mean potential temperature biases of 1–4 K (Fig. 7, top). Because of such biases, it is difficult to plot raw PDFs from multiple models
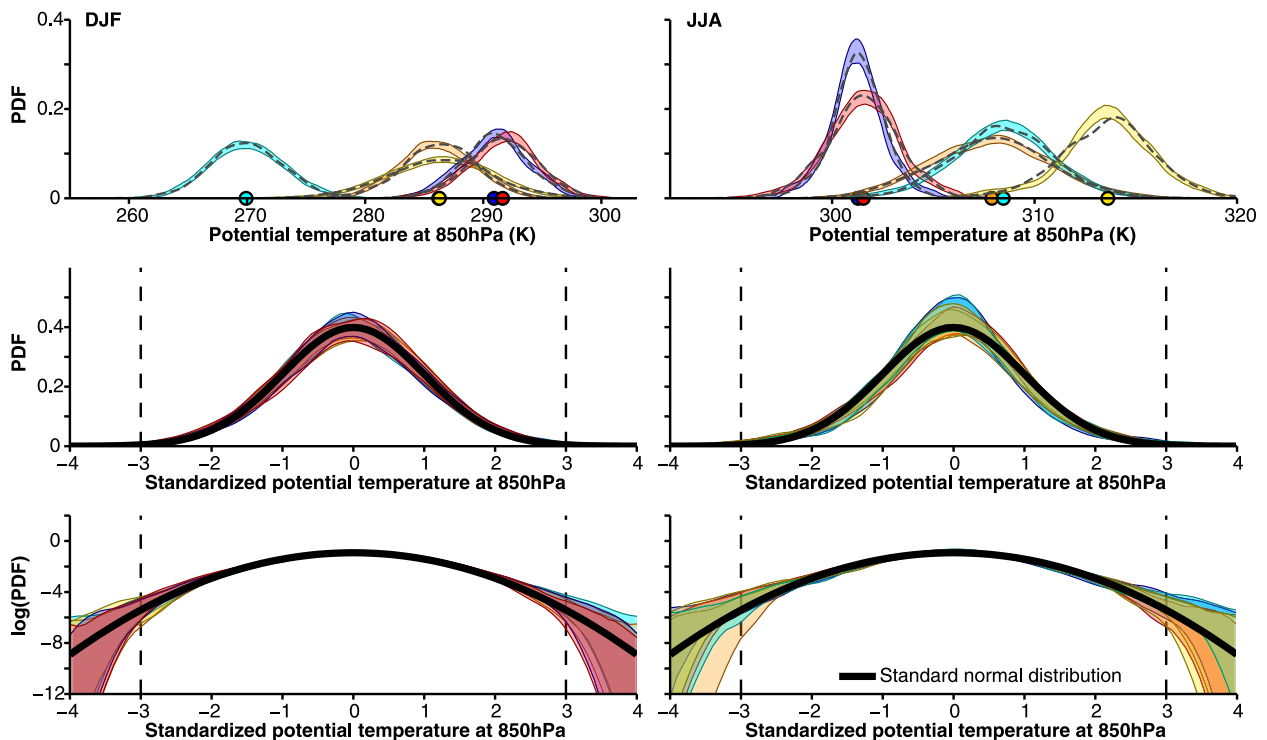
FIG. 8. Estimated PDFs of synoptic 850-hPa potential temperature variations in global-warming (RCP8.5) simulations for 2080–99, at the five representative midlatitude locations in Fig. 1, for (left) DJF and (right) JJA. Color coding of locations, bandpass filtering, and plotting conventions is as in Figs. 2 and 7. (top) Raw PDFs for the Hadley Centre model HadGEM2-CC. The dashed line shows the PDFs that one obtains from the historical PDFs in Fig. 7 if at each location and season the historical PDF is shifted to have the same mean and rescaled to have the same standard deviation as in the RCP8.5 simulations. (middle) PDFs for all models in our ensemble, standardized with the mean and standard deviation for each location, season, and model. (bottom) As in the middle row, but with a logarithmic axis for the PDF.

together. However, once synoptic potential temperature variations are standardized by subtracting the mean and dividing by the standard deviation for each model, location, and season, the distribution of the variations can be compared across models (see appendix A). It is evident that the cores of the multimodel PDFs are essentially Gaussian at all locations (Fig. 7, middle), as they were in the reanalysis (Fig. 2). Plotting the PDFs with a logarithmic axis also shows that the tails of the distributions across models are statistically indistinguishable from Gaussian—again as in the reanalysis.

Figure 8 shows the analogous PDFs of synoptic potential temperature variations in the RCP8.5 simulations. It is clear from the raw PDFs for the Hadley Centre model that the distributions generally shift toward higher temperatures, as one expects under global warming (Fig. 8, top). Some of the variance changes seen in Fig. 6b are also recognizable in the PDFs, for example, a narrowing of the PDF (reduction of variance) in the Pacific storm track in JJA (Fig. 8, purple). If one takes the synoptic potential temperature variations in the historical simulation with the Hadley Centre

model for each location and season and transforms them by shifting the mean and rescaling variations such that they have the same mean and variance as in the RCP8.5 simulation, and if one then estimates the PDFs of those rescaled variations, one obtains the dashed lines in Fig. 8 (top). This simple transformation of synoptic potential temperature variations appears to capture the statistically identifiable changes in the PDFs under global warming. Indeed, the multimodel PDFs of the standardized potential temperature variations across our model ensemble remain statistically indistinguishable from Gaussian, even in the tails (Fig. 8, middle and bottom).

We have verified that changes in the mean and variance account for the changes in the PDFs we see across our model ensemble. The location- and season-specific PDFs of the differences between synoptic potential temperature variations for the years 2080–99 in the RCP8.5 simulations and for the years 1980–99 in the historical simulations are statistically indistinguishable from Gaussian, with a variance equal to the sum of the variances in the historical and RCP8.5 simulations. (The

difference between two Gaussian random variables is also Gaussian. The variance of the difference is equal to the sum of their variances if the two random variables are uncorrelated, which is reasonable to assume for synoptic potential temperature variations in the historical and RCP8.5 simulations.) That is, the statistically identifiable changes in the PDFs of synoptic potential temperature variations under global warming can be attributed to changes in the mean and variance.

We have also verified that the same conclusions hold for air temperatures near the surface, for the subset of models for which daily surface air temperatures were available. In particular, PDFs of synoptic surface air temperature variations are nearly Gaussian to a similar degree as the PDFs of the synoptic potential temperature variations near the surface. However, key for obtaining nearly Gaussian PDFs in either case is to focus on synoptic time scales; otherwise, non-Gaussian features of lower-frequency variability become manifest (see appendix A).

## 6. Summary and discussion

We investigated the physical mechanisms governing changes in synoptic temperature and potential temperature variability near the surface in the midlatitudes. Our principal results can be summarized as follow:

1) To first order, the magnitudes of the meridional potential temperature gradient and of the mixing length determine the synoptic potential temperature variance near the surface in midlatitudes. Arctic amplification of global warming leads to a reduction of the meridional potential temperature gradient that is expected to be larger than any changes in mixing length (especially in winter), leading to a reduction of the synoptic potential temperature variance near the surface.

2) Idealized GCMs and comprehensive climate models robustly show that the synoptic potential temperature variance indeed decreases in midlatitudes of the Northern Hemisphere as the climate warms, especially in winter (when Arctic amplification is strong). Most of that variance reduction can be attributed to a reduction of the meridional potential temperature gradient, consistent with the findings of Screen (2014). But changes in the mixing length and other processes also play a role.

3) In some extratropical regions (e.g., over the Southern Ocean and in central and eastern Europe in summer), the synoptic potential temperature variance increases as the climate warms. This variance increase can at least partially be attributed to a local

strengthening of the meridional potential temperature gradient. As a first step, it may not be necessary to invoke feedback processes beyond those that shape the meridional potential temperature gradient to account for at least part of these variance changes.

4) Probability density functions of synoptic potential temperature variations near the surface in reanalysis data, in idealized GCM simulations, and in comprehensive climate simulations of the present and globally warmer climates are all essentially indistinguishable from Gaussian. This implies that for understanding how the frequency of even rare and large synoptic potential temperature variations changes with climate, at least for now it suffices to understand changes in the mean and variance of the PDFs.

5) On longer time scales ($\gtrsim$25 days), PDFs of near-surface potential temperature variations exhibit non-Gaussian tails, as seen in recent studies of surface temperature variations (e.g., Ruff and Neelin 2012; Huybers et al. 2014; Loikith et al. 2015). PDFs with sub-Gaussian tails are especially prevalent and imply that nonlinear processes must be operating that damp large deviations relative to normal statistics.

6) Idealized GCM simulations show that interactions of orographic stationary waves with transient eddies do not generally modify the response of synoptic near-surface potential temperature variations to climate change substantially.

Taken together, these findings indicate that Arctic amplification of global warming leads to even less frequent cold outbreaks in the Northern Hemispheric winter than are already implied by a shift toward a warmer mean climate. We did not examine specifically how the frequency of blocking episodes changes with climate (cf. Liu et al. 2012; Hassanzadeh et al. 2014). However, our analyses suggest they do not modify synoptic potential temperature variations and/or their departures from Gaussian statistics substantially.

Our results leave open the possibility that changes in atmospheric stationary waves under global warming modulate midlatitude weather variability regionally. For example, there is evidence that enhanced convective activity over the tropical Pacific Ocean enhances stationary Rossby waves radiating from that region into the midlatitudes, modulating weather variability, for example, over North America (Palmer and Mansfield 1984; Palmer and Owen 1986; Meehl and Tebaldi 2004; Palmer 2014; Simpson et al. 2014). Similar stationary wave connections may originate in other regions and may be linked, for example, to Arctic sea ice retreat (e.g., Peings and Magnusdottir 2014; Simmonds and Govekar 2014; Screen and Simmonds 2014). Our study

did not address such changes in stationary waves. Our results also leave open the possibility that land–atmosphere and other feedbacks may affect the global-warming response of near-surface temperature variability, either by the feedbacks modifying the mean near-surface temperatures and potential temperatures and their gradients, or by the feedbacks directly modifying the variances. Such feedbacks—both positive and negative—may be particularly important on longer time scales than the synoptic time scales on which we have focused. On synoptic time scales, the Gaussianity of the statistics indicates that efforts should be focused primarily on understanding what controls the response of the mean near-surface temperature and potential temperature to global warming, and on how this mean response, through gradient changes and other processes, impacts the variance response.

# APPENDIX A

## Bandpass Filtering and Estimation of PDFs

Potential temperature variations from reanalyses, the idealized GCM, and the comprehensive CMIP5 simulations were processed in the same way, first by bandpass filtering them and then by estimating PDFs from the bandpass-filtered variations. We used daily potential temperature variations for the ERA-Interim data and CMIP5 simulations. We used four times daily potential temperature variations for the idealized GCM simulations.

### a. Bandpass filtering

We bandpass filter the time series $\theta(t)$ of potential temperature variations at each location by computing the discrete Fourier transform $\hat{\theta}(\nu)$, with frequency $\nu$, then zeroing coefficients $\hat{\theta}(\nu)$ corresponding to periods $2\pi/\nu < 3$ days and $2\pi/\nu > 15$ days, before transforming back to real space. We have experimented with different forms of filtering and have tested the sensitivity of our results to the cutoff frequencies. None of the results we presented are sensitive to details of the filtering.

However, if variability with substantially longer time scales is included, PDFs can have non-Gaussian features. For example, Fig. A1 shows the PDFs analogous to Fig. 2 but for potential temperature variations bandpass filtered to time scales of 25–35 days. It is clear that these lower-frequency variations at several locations exhibit sub-Gaussian tails, and some have sizable kurtosis. For some PDFs, the tails are skewed toward large warm deviations occurring more frequently than large cold deviations (e.g., over the Pacific in DJF; purple in Fig. A1). PDFs of surface air temperature bandpass filtered to such longer time scales exhibit similar features. They are also seen in PDFs of unfiltered daily variations, to which the low-frequency variations contribute, both in the observations and simulations (Fischer and Schär 2009; Ruff and Neelin 2012; Huybers et al. 2014; Loikith et al. 2015).

### b. Estimation of PDFs

We estimate PDFs using a Gaussian kernel density estimator (Bowman and Azzalini 1997):

$$\hat{f}_h(x) = \frac{1}{nh} \sum_{i=1}^{n} K\left(\frac{x - x_i}{h}\right),$$

where $n$ is the sample size, $h$ is the bandwidth (a smoothing parameter), and the kernel

$$K(u) = \frac{1}{\sqrt{2\pi}} e^{-u^2/2}$$

is the standard normal distribution. The bandwidth $h$ is chosen to minimize the mean integrated squared error if the data were Gaussian, which gives

$$h = \left(\frac{4\sigma^5}{3n}\right)^{1/5},$$

where $\sigma$ is the standard deviation of the sample (Silverman 1986).

### c. Bootstrap confidence intervals

To obtain confidence intervals for the estimated PDFs, we use a bootstrap procedure (Efron 1979; Efron and Tibshirani 1993). We resample with replacement
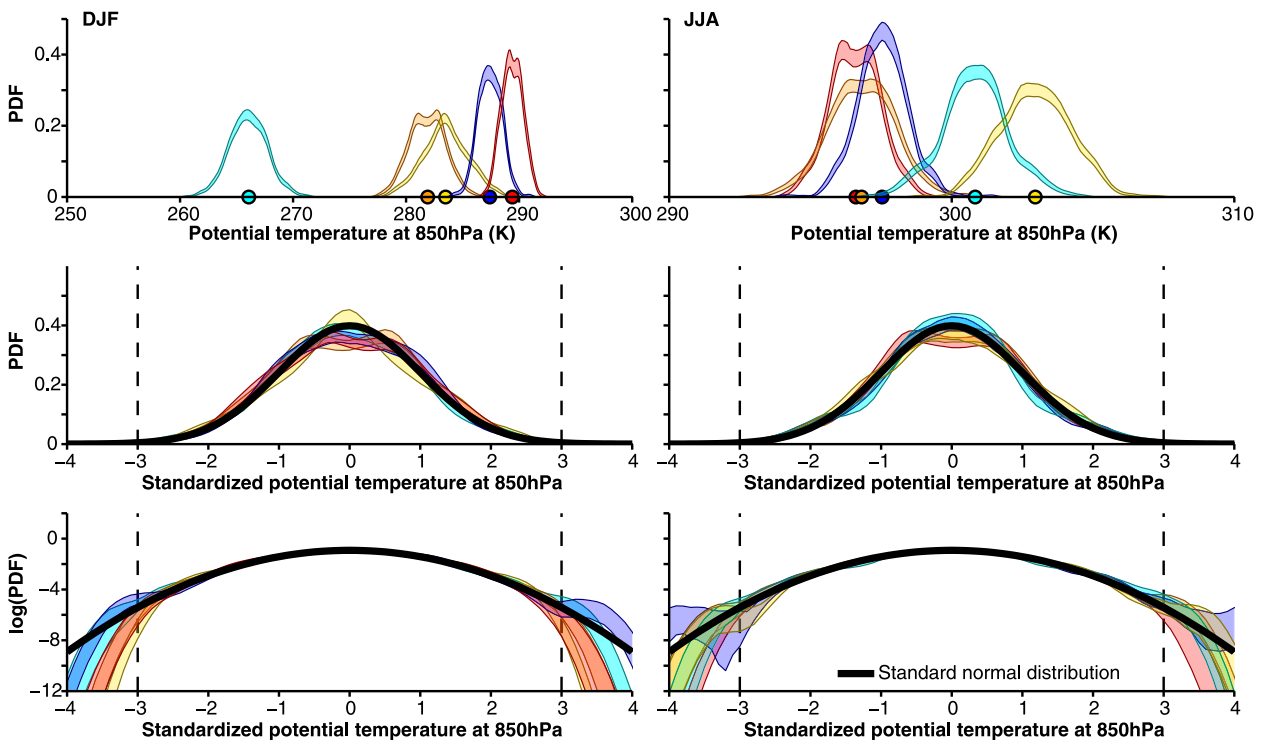
FIG. A1. Estimated PDFs of 850-hPa potential temperature variations bandpass filtered to 25–35-day time scales, at the same five midlatitude locations for which synoptic PDFs are shown in Fig. 2. Except for the different bandpass filtering, all other conventions are as in Fig. 2.

from our original data $S_o$ to construct a bootstrap sample $S_b$ of the same size as $S_o$, but differing from $S_o$ in that each point in $S_o$ may appear in $S_b$ more than once or not at all. From the bootstrap sample, we reestimate a PDF as described above, and we repeat this $n_b = 200$ times. This gives $n_b$-estimated PDFs, from which we construct pointwise 95% confidence intervals by taking the 2.5th and 97.5th percentiles of the distribution of PDFs at each point. Because this procedure neglects temporal correlations in the underlying time series (bootstrap samples are drawn without regard for the temporal order of the underlying time series), it overestimates the effective sample size and therefore likely underestimates the width of the confidence intervals. Nonetheless, even with the likely overly narrow confidence intervals, almost all estimated PDFs are statistically indistinguishable from Gaussian.

For the reanalysis data, for the idealized GCM simulations, and for the climate model in the top rows of Figs. 7 and 8, we drew $n_b$ bootstrap samples from the synoptic potential temperature variations for each location and each season and estimated PDFs and confidence intervals from them. For the ensemble of CMIP5 simulations in the middle and bottom rows of Figs. 7 and 8, we drew $n_b$ bootstrap samples for each model,

location, and season; standardized the synoptic potential temperature variations for each model, location, and season; and then pooled the standardized variations of all models into one large sample, from which we estimated PDFs and confidence intervals.

## APPENDIX B

### Idealized GCM Simulations

#### a. GCM setup

The idealized GCM used in this study is similar to that in Frierson et al. (2006) and O'Gorman and Schneider (2008b) but with a simple representation of coupled ocean heat transport in low latitudes, as in Levine and Schneider (2011). The GCM has a simplified representation of the hydrological cycle, taking into account only the liquid-vapor phase transition and neglecting the ice phase of water. The latent heat of evaporation is assumed to be independent of temperature with a value that is fixed at $L_v = 2.5 \times 10^6 \, \mathrm{J \, kg^{-1}}$. The convection scheme is similar to the quasi-equilibrium scheme described in Frierson (2007).

The GCM employs a two-stream radiation scheme with fixed optical depth profiles. Representing

approximately the annual mean, the top-of-the-atmosphere insolation is prescribed as

$$\mathcal{S} = \frac{S_0}{4}\left[1 + \frac{\Delta_s}{4}(1 - 3\sin^2\phi)\right], \quad \text{(B1)}$$

where $S_0 = 1360\,\mathrm{W\,m^{-2}}$ is the solar constant, and $\Delta_s = 1.2$ is a dimensionless measure of the insolation gradient. With increasing pressure $p$, shortwave radiation in the atmosphere is attenuated by an exponential factor of $\exp[-\tau_s(p/p_s)^2]$, with shortwave optical thickness $\tau_s = 0.22$. Dynamic radiative water vapor feedbacks and cloud feedbacks are neglected.

As in O'Gorman and Schneider (2008b), longwave radiation is absorbed by an idealized absorber with an optical depth $\tau_l = \alpha\tau_{\mathrm{ref}}(\phi)$, where $\alpha$ is a rescaling factor that is varied in the global-warming simulations to rescale the reference optical depth:

$$\tau_{\mathrm{ref}} = [f_l\sigma + (1 - f_l)\sigma^4][\tau_e + (\tau_p - \tau_e)\sin^2\phi]. \quad \text{(B2)}$$

Here, $f_l = 0.2$ measures the fraction of the absorber whose optical depth increases linearly with $p/p_s$ (representing an approximately well-mixed absorber) and $1 - f_l$ is the fraction of the water-vapor-like absorber whose optical depth increases quartically with $p/p_s$. Here, $\tau_e = 7.2$ is the longwave optical depth at the equator and $\tau_p = 1.8$ is that at the poles.

The Southern Hemisphere of the idealized GCM has no topography. In the Northern Hemisphere, we introduce a Gaussian mountain, which is 4 km high and centered at 45°N. Zonally, it falls off following a Gaussian with a standard deviation of 15° longitude to excite zonal wavenumber 6–8 stationary waves. Meridionally, the mountain has a ridge extending ±2.5° north and south of 45°N, before falling off following a Gaussian with standard deviation of 5° latitude.

*b. Simulations*

We simulated a wide range of climates by varying the rescaling parameter $\alpha$ of the reference longwave optical thickness. We vary $\alpha$ between 0.4 and 4.0 (six simulations). This range of climates is similar to the range explored in O'Gorman and Schneider (2008b) and results in global-mean surface temperatures that range from 273 to 310 K. All simulations are run at spectral T127 horizontal resolution and with 30 $\sigma$ levels in the vertical. The simulations are spun up for 1880 simulated days, until a statistically steady state was reached. The statistics shown here were accumulated over an additional 1800 days.

## REFERENCES

Barnes, E. A., 2013: Revisiting the evidence linking Arctic amplification to extreme weather in midlatitudes. *Geophys. Res. Lett.,* **40,** 4734–4739, doi:10.1002/grl.50880.

——, E. Dunn-Sigouin, G. Masato, and T. Woollings, 2014: Exploring recent trends in Northern Hemisphere blocking. *Geophys. Res. Lett.,* **41,** 638–644, doi:10.1002/2013GL058745.

Bennett, A. F., 1987: A Lagrangian analysis of turbulent diffusion. *Rev. Geophys.,* **25,** 799–822, doi:10.1029/RG025i004p00799.

Berg, A., B. R. Lintner, K. L. Findell, S. Malyshev, P. C. Loikith, and P. Gentine, 2014: Impact of soil moisture–atmosphere interactions on surface temperature distribution. *J. Climate,* **27,** 7976–7993, doi:10.1175/JCLI-D-13-00591.1.

Boer, G. J., and T. G. Shepherd, 1983: Large-scale two-dimensional turbulence in the atmosphere. *J. Atmos. Sci.,* **40,** 164–184, doi:10.1175/1520-0469(1983)040<0164:LSTDTI>2.0.CO;2.

Booth, J. F., L. Polvani, P. A. O'Gorman, and S. Wang, 2015: Effective stability in a moist baroclinic wave. *Atmos. Sci. Lett.,* **16,** 56–62, doi:10.1002/asl2.520.

Bowman, A. W., and A. Azzalini, 1997: *Applied Smoothing Techniques for Data Analysis: The Kernel Approach with S-Plus Illustrations.* Oxford Statistical Science Series, Vol. 18, Oxford University Press, 204 pp.

Cohen, J., and Coauthors, 2014: Recent Arctic amplification and extreme mid-latitude weather. *Nat. Geosci.,* **7,** 627–637, doi:10.1038/ngeo2234.

Collins, M., and Coauthors, 2013: Long-term climate change: Projections, commitments and irreversibility. *Climate Change 2013: The Physical Science Basis,* T. F. Stocker et al., Eds., Cambridge University Press, 1029–1136.

Corrsin, S., 1974: Limitations of gradient transport models in random walks and in turbulence. *Advances in Geophysics,* Vol. 18A, Academic Press, 25–60.

Coumou, D., A. Robinson, and S. Rahmstorf, 2013: Global increase in record-breaking monthly-mean temperatures. *Climatic Change,* **118,** 771–782, doi:10.1007/s10584-012-0668-1.

——, V. Petoukhov, S. Rahmstorf, S. Petri, and H. J. Schellnhuber, 2014: Quasi-resonant circulation regimes and hemispheric synchronization of extreme weather in boreal summer. *Proc. Natl. Acad. Sci. USA,* **111,** 12 331–12 336, doi:10.1073/pnas.1412797111.

Daoud, W. Z., J. D. W. Kahl, and J. K. Ghorai, 2003: On the synoptic-scale Lagrangian autocorrelation function. *J. Appl. Meteor.,* **42,** 318–324, doi:10.1175/1520-0450(2003)042<0318:OTSSLA>2.0.CO;2.

Dee, D. P., and Coauthors, 2011: The ERA-Interim reanalysis: Configuration and performance of the data assimilation system. *Quart. J. Roy. Meteor. Soc.,* **137,** 553–597, doi:10.1002/qj.828.

de Vries, H., R. J. Haarsma, and W. Hazeleger, 2012: Western European cold spells in current and future climate. *Geophys. Res. Lett.,* **39,** L04706, doi:10.1029/2011GL050665.

Donat, M. G., and L. V. Alexander, 2012: The shifting probability distribution of global daytime and night-time temperatures. *Geophys. Res. Lett.,* **39,** L14707, doi:10.1029/2012GL052459.

Easterling, D. R., G. A. Meehl, C. Parmesan, S. A. Changnon, T. R. Karl, and L. O. Mearns, 2000: Climate extremes: Observations, modeling, and impacts. *Science,* **289,** 2068–2074, doi:10.1126/science.289.5487.2068.

Efron, B., 1979: Bootstrap methods: Another look at the jackknife. *Ann. Stat.,* **7,** 1–26, doi:10.1214/aos/1176344552.

——, and R. J. Tibshirani, 1993: *An Introduction to the Bootstrap.* Monographs on Statistics and Applied Probability, Vol. 57, Chapman and Hall, 456 pp.

Fischer, E. M., and C. Schär, 2009: Future changes in daily summer temperature variability: Driving processes and role for temperature extremes. *Climate Dyn., 33,* 917–935, doi:10.1007/s00382-008-0473-8.

Francis, J. A., and S. J. Vavrus, 2012: Evidence linking Arctic amplification to extreme weather in mid-latitudes. *Geophys. Res. Lett., 39,* L06801, doi:10.1029/2012GL051000.

Frierson, D. M. W., 2007: The dynamics of idealized convection schemes and their effect on the zonally averaged tropical circulation. *J. Atmos. Sci., 64,* 1959–1976, doi:10.1175/JAS3935.1.

——, 2008: Midlatitude static stability in simple and comprehensive general circulation models. *J. Atmos. Sci., 65,* 1049–1062, doi:10.1175/2007JAS2373.1.

——, I. M. Held, and P. Zurita-Gotor, 2006: A gray-radiation aquaplanet moist GCM. Part I: Static stability and eddy scale. *J. Atmos. Sci., 63,* 2548–2566, doi:10.1175/JAS3753.1.

Graversen, R. G., T. Mauritsen, M. Tjernström, E. Källén, and G. Svensson, 2008: Vertical structure of recent arctic warming. *Nature, 541,* 53–56, doi:10.1038/nature06502.

Gregory, J. M., and J. F. B. Mitchell, 1995: Simulation of daily variability of surface temperature and precipitation over Europe in the current and $2 \times CO_2$ climates using the UKMO climate model. *Quart. J. Roy. Meteor. Soc., 121,* 1451–1476.

Hansen, J., M. Sato, and R. Ruedy, 2012: Perception of climate change. *Proc. Natl. Acad. Sci. USA, 109,* E2415–E2423, doi:10.1073/pnas.1205276109.

Hassanzadeh, P., Z. Kuang, and B. F. Farrell, 2014: Responses of midlatitude blocks and wave amplitude to changes in the meridional temperature gradient in an idealized dry GCM. *Geophys. Res. Lett., 41,* 5223–5232, doi:10.1002/2014GL060764.

Held, I. M., 1999: The macroturbulence of the troposphere. *Tellus, 51A,* 59–70, doi:10.1034/j.1600-0870.1999.t01-1-00006.x.

——, and V. D. Larichev, 1996: A scaling theory for horizontally homogeneous, baroclinically unstable flow on a beta-plane. *J. Atmos. Sci., 53,* 946–952, doi:10.1175/1520-0469(1996)053<0946:ASTFHH>2.0.CO;2.

Holdren, J., cited 2014: The polar vortex explained in 2 minutes. [Available online at http://www.whitehouse.gov/photos-and-video/video/2014/01/08/polar-vortex-explained-2-minutes.]

Holland, M. M., and C. M. Bitz, 2003: Polar amplification of climate change in coupled models. *Climate Dyn., 21,* 221–232, doi:10.1007/s00382-003-0332-6.

Huntingford, C., P. D. Jones, V. N. Livina, T. M. Lenton, and P. M. Cox, 2013: No increase in global temperature variability despite changing regional patterns. *Nature, 500,* 327–330, doi:10.1038/nature12310.

Huybers, P., K. A. McKinnon, A. Rhines, and M. Tingley, 2014: U.S. daily temperatures: The meaning of extremes in the context of nonnormality. *J. Climate, 27,* 7368–7384, doi:10.1175/JCLI-D-14-00216.1.

Keppel-Aleks, G., P. O. Wennberg, and T. Schneider, 2011: Sources of variations in total column carbon dioxide. *Atmos. Chem. Phys., 11,* 3581–3593, doi:10.5194/acp-11-3581-2011.

——, and Coauthors, 2012: The imprint of surface fluxes and transport on variations in total column carbon dioxide. *Biogeosciences, 9,* 875–891, doi:10.5194/bg-9-875-2012.

Kidston, J., S. M. Dean, J. A. Renwick, and G. K. Vallis, 2010: A robust increase in the eddy length scale in the simulation of future climates. *Geophys. Res. Lett., 37,* L03806, doi:10.1029/2009GL041615.

Kimura, Y., and R. H. Kraichnan, 1993: Statistics of an advected passive scalar. *Phys. Fluids A, 5,* 2264–2277, doi:10.1063/1.858530.

Kintisch, E., 2014: Into the maelstrom. *Science, 344,* 250–253, doi:10.1126/science.344.6181.250.

Kitoh, A., and T. Mukano, 2009: Changes in daily and monthly surface air temperature variability by multi-model global warming experiments. *J. Meteor. Soc. Japan, 87,* 513–524, doi:10.2151/jmsj.87.513.

Kushner, P. J., and I. M. Held, 1998: A test, using atmospheric data, of a method for estimating oceanic eddy diffusivity. *Geophys. Res. Lett., 25,* 4213–4216, doi:10.1029/1998GL900142.

Levine, X. J., and T. Schneider, 2011: Response of the Hadley circulation to climate change in an aquaplanet GCM coupled to a simple representation of ocean heat transport. *J. Atmos. Sci., 68,* 769–783, doi:10.1175/2010JAS3553.1.

Liu, J., J. A. Curry, H. Wang, M. Song, and R. M. Horton, 2012: Impact of declining Arctic sea ice on winter snowfall. *Proc. Natl. Acad. Sci. USA, 109,* 4074–4079, doi:10.1073/pnas.1114910109.

Loikith, P. C., and Coauthors, 2015: Surface temperature probability distributions in the NARCCAP hindcast experiment: Evaluation methodology, metrics, and results. *J. Climate, 28,* 978–997, doi:10.1175/JCLI-D-13-00457.1.

Manabe, S., and R. T. Wetherald, 1980: On the distribution of climate change resulting from an increase in $CO_2$ content of the atmosphere. *J. Atmos. Sci., 37,* 99–118, doi:10.1175/1520-0469(1980)037<0099:OTDOCC>2.0.CO;2.

Masson-Delmotte, V., and Coauthors, 2013: Information from paleoclimate archives. *Climate Change 2013: The Physical Science Basis,* T. F. Stocker et al., Eds., Cambridge University Press, 383–464.

Mbengue, C., and T. Schneider, 2013: Storm track shifts under climate change: What can be learned from large-scale dry dynamics. *J. Climate, 26,* 9923–9930, doi:10.1175/JCLI-D-13-00404.1.

Meehl, G. A., and C. Tebaldi, 2004: More intense, more frequent, and longer lasting heat waves in the 21st century. *Science, 305,* 994–997, doi:10.1126/science.1098704.

Merlis, T. M., and T. Schneider, 2009: Scales of linear baroclinic instability and macroturbulence in dry atmospheres. *J. Atmos. Sci., 66,* 1821–1833, doi:10.1175/2008JAS2884.1.

O'Gorman, P. A., 2010: Understanding the varied response of the extratropical storm tracks to climate change. *Proc. Natl. Acad. Sci. USA, 107,* 19 176–19 180, doi:10.1073/pnas.1011547107.

——, 2011: The effective static stability experienced by eddies in a moist atmosphere. *J. Atmos. Sci., 68,* 75–90, doi:10.1175/2010JAS3537.1.

——, and T. Schneider, 2008a: Energy of midlatitude transient eddies in idealized simulations of changed climates. *J. Climate, 21,* 5797–5806, doi:10.1175/2008JCLI2099.1.

——, and ——, 2008b: The hydrological cycle over a wide range of climates simulated with an idealized GCM. *J. Climate, 21,* 3815–3832, doi:10.1175/2007JCLI2065.1.

Palmer, T. N., 2014: Record-breaking winters and global climate change. *Science, 344,* 803–804, doi:10.1126/science.1255147.

——, and D. A. Mansfield, 1984: Response of two atmospheric general circulation models to sea-surface temperature anomalies in the tropical East and West Pacific. *Nature, 310,* 483–485, doi:10.1038/310483a0.

——, and J. A. Owen, 1986: A possible relationship between some severe winters in North America and enhanced convective activity over the tropical West Pacific. *Mon. Wea.*

*Rev.,* **114,** 648–651, doi:10.1175/1520-0493(1986)114<0648: APRBSW>2.0.CO;2.

Peings, Y., and G. Magnusdottir, 2014: Response of the wintertime Northern Hemisphere atmospheric circulation to current and projected Arctic sea ice decline: A numerical study with CAM5. *J. Climate,* **27,** 244–264, doi:10.1175/JCLI-D-13-00272.1.

Peterson, T. C., and Coauthors, 2013: Monitoring and understanding changes in heat waves, cold waves, floods, and droughts in the United States: State of knowledge. *Bull. Amer. Meteor. Soc.,* **94,** 821–834, doi:10.1175/BAMS-D-12-00066.1.

Petoukhov, V., S. Rahmstorf, S. Petria, and H. J. Schellnhuber, 2013: Quasiresonant amplification of planetary waves and recent Northern Hemisphere weather extremes. *Proc. Natl. Acad. Sci. USA,* **110,** 5336–5341, doi:10.1073/pnas.1222000110.

Pierrehumbert, R. T., 2000: Lattice models of advection-diffusion. *Chaos,* **10,** 61–74, doi:10.1063/1.166476.

Pumir, A., B. Shraiman, and E. D. Siggia, 1991: Exponential tails and random advection. *Phys. Rev. Lett.,* **66,** 2984–2987, doi:10.1103/PhysRevLett.66.2984.

Rhines, A., and P. Huybers, 2013: Frequent summer temperature extremes reflect changes in the mean, not the variance. *Proc. Natl. Acad. Sci. USA,* **110,** E546, doi:10.1073/pnas.1218748110.

Riahi, K., and Coauthors, 2011: RCP8.5—A scenario of comparatively high greenhouse gas emissions. *Climatic Change,* **109,** 33–57, doi:10.1007/s10584-011-0149-y.

Ruff, T. W., and J. D. Neelin, 2012: Long tails in regional surface temperature probability distributions with implications for extremes under global warming. *Geophys. Res. Lett.,* **39,** L04704, doi:10.1029/2011GL050610.

Schär, C., P. L. Vidale, D. Lüthi, C. Frei, C. Häberli, M. A. Liniger, and C. Appenzeller, 2004: The role of increasing temperature variability in European summer heatwaves. *Nature,* **427,** 332–336, doi:10.1038/nature02300.

Schneider, T., 2007: The thermal stratification of the extratropical troposphere. *The Global Circulation of the Atmosphere,* T. Schneider and A. H. Sobel, Eds., Princeton University Press, 47–77.

——, and I. M. Held, 2001: Discriminants of twentieth-century changes in Earth surface temperatures. *J. Climate,* **14,** 249–254, doi:10.1175/1520-0442(2001)014<0249:LDOTCC>2.0.CO;2.

——, and C. C. Walker, 2006: Self-organization of atmospheric macroturbulence into critical states of weak nonlinear eddy–eddy interactions. *J. Atmos. Sci.,* **63,** 1569–1586, doi:10.1175/JAS3699.1.

——, and P. A. O'Gorman, 2008: Moist convection and the thermal stratification of the extratropical troposphere. *J. Atmos. Sci.,* **65,** 3571–3583, doi:10.1175/2008JAS2652.1.

——, and C. C. Walker, 2008: Scaling laws and regime transitions of macroturbulence in dry atmospheres. *J. Atmos. Sci.,* **65,** 2153–2173, doi:10.1175/2007JAS2616.1.

——, P. A. O'Gorman, and X. J. Levine, 2010: Water vapor and the dynamics of climate changes. *Rev. Geophys.,* **48,** RG3001, doi:10.1029/2009RG000302.

Screen, J. A., 2014: Arctic amplification decreases temperature variance in northern mid- to high-latitudes. *Nat. Climate Change,* **4,** 577–582, doi:10.1038/nclimate2268.

——, and I. Simmonds, 2010: The central role of diminishing sea ice in recent Arctic temperature amplification. *Nature,* **464,** 1334–1337, doi:10.1038/nature09051.

——, and ——, 2013a: Caution needed when linking weather extremes to amplified planetary waves. *Proc. Natl. Acad. Sci. USA,* **110,** E2327, doi:10.1073/pnas.1304867110.

——, and ——, 2013b: Exploring links between Arctic amplification and mid-latitude weather. *Geophys. Res. Lett.,* **40,** 959–964, doi:10.1002/grl.50174.

——, and ——, 2014: Amplified mid-latitude planetary waves favour particular regional weather extremes. *Nat. Climate Change,* **4,** 704–709, doi:10.1038/nclimate2271.

——, C. Deser, and I. Simmonds, 2012: Local and remote controls on observed Arctic warming. *Geophys. Res. Lett.,* **39,** L10709, doi:10.1029/2012GL051598.

——, ——, and L. Sun, 2015: Reduced risk of North American cold extremes due to continued Arctic sea ice loss. *Bull. Amer. Meteor. Soc.,* doi:10.1175/BAMS-D-14-00185.1, in press.

Seneviratne, S. I., D. Lüthi, M. Litschi, and C. Schär, 2006: Land–atmosphere coupling and climate change in Europe. *Nature,* **443,** 205–209, doi:10.1038/nature05095.

——, T. Corti, E. L. Davin, M. Hirschi, E. B. Jaeger, I. Lehner, B. Orlowsky, and A. J. Teuling, 2010: Investigating soil moisture–climate interactions in a changing climate: A review. *Earth Sci. Rev.,* **99,** 125–161, doi:10.1016/j.earscirev.2010.02.004.

Serreze, M. C., and R. G. Barry, 2011: Processes and impacts of Arctic amplification: A research synthesis. *Global Planet. Change,* **77,** 85–96, doi:10.1016/j.gloplacha.2011.03.004.

Shepherd, T. G., 1987: A spectral view of nonlinear fluxes and stationary-transient interaction in the atmosphere. *J. Atmos. Sci.,* **44,** 1166–1178, doi:10.1175/1520-0469(1987)044<1166: ASVONF>2.0.CO;2.

Shraiman, B. I., and E. D. Siggia, 1994: Lagrangian path integrals and fluctuations in random flow. *Phys. Rev.,* **49E,** 2912–2927.

——, and ——, 2000: Scalar turbulence. *Nature,* **405,** 639–646, doi:10.1038/35015000.

Silverman, B. W., 1986: *Density Estimation for Statistics and Data Analysis.* Chapman and Hall, 175 pp.

Simmonds, I., and P. D. Govekar, 2014: What are the physical links between Arctic sea ice loss and Eurasian winter climate? *Environ. Res. Lett.,* **9,** 101003, doi:10.1088/1748-9326/9/10/101003.

Simpson, I. R., T. A. Shaw, and R. Seager, 2014: A diagnosis of the seasonally and longitudinally varying midlatitude circulation response to global warming. *J. Atmos. Sci.,* **71,** 2489–2515, doi:10.1175/JAS-D-13-0325.1.

Swanson, K. L., and R. T. Pierrehumbert, 1997: Lower-tropospheric heat transport in the Pacific storm track. *J. Atmos. Sci.,* **54,** 1533–1543, doi:10.1175/1520-0469(1997)054<1533: LTHTIT>2.0.CO;2.

Taylor, G. I., 1921: Diffusion by continuous movements. *Proc. London Math. Soc.,* **20,** 196–211.

Taylor, K. E., R. J. Stouffer, and G. A. Meehl, 2012: An overview of CMIP5 and the experiment design. *Bull. Amer. Meteor. Soc.,* **93,** 485–498, doi:10.1175/BAMS-D-11-00094.1.

Thuburn, J., and G. C. Craig, 2000: Stratospheric influence on tropopause height: The radiative constraint. *J. Atmos. Sci.,* **57,** 17–28, doi:10.1175/1520-0469(2000)057<0017: SIOTHT>2.0.CO;2.

Tingley, M. P., and P. Huybers, 2013: Recent temperature extremes at high northern latitudes unprecedented in the past 600 years. *Nature,* **496,** 201–205, doi:10.1038/nature11969.

Wallace, J. M., I. M. Held, D. W. J. Thompson, K. E. Trenberth, and J. E. Walsh, 2014: Global warming and winter weather. *Science,* **343,** 729–730, doi:10.1126/science.343.6172.729.

Warhaft, Z., 2000: Passive scalars in turbulent flows. *Annu. Rev. Fluid Mech.,* **32,** 203–240, doi:10.1146/annurev.fluid.32.1.203.

Ylhäisi, J. S., and J. Räisänen, 2014: Twenty-first century changes in daily temperature variability in CMIP3 climate models. *Int. J. Climatol.,* **34,** 1414–1428, doi:10.1002/joc.3773.